



LAWRENCE
LIVERMORE
NATIONAL
LABORATORY

A New Approach to the Evaluation and Solution of the Relativistic Kinetic Dispersion Relation, and Verification with Continuum Kinetic Simulation

W. J. Arrighi, J. W. Banks, R. L. Berger, T. Chapman, A. Gianesini Odu, J. Gorman

January 22, 2024

Journal of Computational Physics

Disclaimer

This document was prepared as an account of work sponsored by an agency of the United States government. Neither the United States government nor Lawrence Livermore National Security, LLC, nor any of their employees makes any warranty, expressed or implied, or assumes any legal liability or responsibility for the accuracy, completeness, or usefulness of any information, apparatus, product, or process disclosed, or represents that its use would not infringe privately owned rights. Reference herein to any specific commercial product, process, or service by trade name, trademark, manufacturer, or otherwise does not necessarily constitute or imply its endorsement, recommendation, or favoring by the United States government or Lawrence Livermore National Security, LLC. The views and opinions of authors expressed herein do not necessarily state or reflect those of the United States government or Lawrence Livermore National Security, LLC, and shall not be used for advertising or product endorsement purposes.

A New Approach to the Evaluation and Solution of the Relativistic Kinetic Dispersion Relation and Verification with Continuum Kinetic Simulation

W. J. Arrighi^{a,1}, J. W. Banks^{b,1,*}, R. L. Berger^{a,1}, T. Chapman^{a,1}, A. Ganesini Odu^b, J. Gorman^{b,1}

^a*Lawrence Livermore National Laboratory, P.O. Box 808, Livermore, CA USA*

^b*Department of Mathematical Sciences, Rensselaer Polytechnic Institute, Troy, NY 12180, USA*

Abstract

The present work describes a new approach to evaluation and root finding for the kinetic dispersion relation of Langmuir waves, which is central to the analytical understanding of collisionless damping in plasmas. The plasma dispersion function is solved to machine precision using direct integration in the complex plane in combination with an analytic evaluation of the residue to account for the deformation along the Landau contour. To efficiently attain machine precision, the contour is displaced in the complex plane prior to integration, and numerical subtleties related to the placement of the contour are discussed. The approach is generic in that it applies to arbitrary distribution functions, with the present manuscript focused on relativistic cases. Detailed verification of results via direct kinetic simulation in a variety of configuration space dimensions is also presented. Finally, the technique is applied to the challenging case of highly relativistic (i.e. extremely hot) plasmas. Here we show both qualitative agreement with prior work, as well as the disappearance of the the Landau root which would have significant implication for real-life observation or experiment.

Keywords: Landau damping, kinetic dispersion relation, relativity, kinetic simulation

1. Introduction

Kinetic effects are important in a wide variety of physics application including inertial confinement devices [1, 2], magnetic confinement devices [3, 4], space plasmas [5, 6], laser wakefield acceleration [7, 8], and even galactic dynamics [9] to name a few. In the present work, “kinetic” indicates a process whose dynamics are described with independent variables of space and momentum, as opposed to so-called fluid models with just spatial independent variables, e.g. moment-reduced fluid equations. Kinetic equations arise because for a classical N -particle system where quantum effects are negligible, the precise motion of all N particles and any associated electromagnetic fields constitutes a complete description of the system. However, the majority of applications contain such a large number of particles that they cannot be practically tracked (i.e. available and foreseeable computing resources are simply insufficient). From a simulation point of view, one is therefore constrained to either consider an approximation using a smaller number of particles (sometimes thought of as macro-particles), or to consider the number of particles to be so large that

*Corresponding author

Email addresses: arrighi2@llnl.gov (W. J. Arrighi), banksj3@rpi.edu (J. W. Banks), berger5@llnl.gov (R. L. Berger), chapman29@llnl.gov (T. Chapman), gormaj4@rpi.edu (J. Gorman)

¹This work was performed under the auspices of the U.S. Department of Energy by Lawrence Livermore National Laboratory under Contract DE-AC52-07NA27344 and was funded by the Laboratory Research and Development Program at the LLNL under Project Tracking Code Number 22-ERD-042.

the limit $N \rightarrow \infty$ is a sensible approximation. The former leads to the well-known particle-in-cell description [10], and the later to a continuum kinetic descriptions such as the Vlasov or Boltzmann equations.

The focus of the present work is the Vlasov equation, which is a continuum kinetic description of collisionless plasmas. An important phenomenon in kinetic physics is the presence of Landau (collisionless) damping, whereby the fluctuating electric field in a collisionless plasma exhibits exponential damping in time. This despite the fact that the governing equations are strictly time-reversible, which would indicate that solutions to the system would be purely undamped. A key breakthrough in the theory was originally discussed in [11], and subsequently by a many authors including vanKampen [12], and Cédric Villani who was awarded the Fields Medal partly for “his proofs of nonlinear Landau damping” [13].

Landau damping of electrostatic waves was investigated experimentally in [14], and has been subsequently probed in numerous experiments, e.g. [15–17]. The existence of Landau damping is now assumed, and is used for example in the theory of wave heating and current drive of Tokamaks[18–23]. Similarly for prediction of parametric instability in inertial fusion hohlraums, growth thresholds are determined using a combination of plasma inhomogeneities and wave both collisional and Landau damping [24–27]. Application of this work to specific experiments on large scale facilities enabled detailed analysis of results and, subsequently, to the development of numerical codes that are routinely used to design experiments for current drive [28] and for ICF that avoid instability by maximizing Landau damping [29–34]. These works all assumed the plasma was hot (2-5 keV) but below the range where the wave interacted with relativistic electrons. Recent experiments, however, have created plasmas with electron temperatures reaching up to 10 keV,[35, 36] where non-relativistic theory would predict stronger Landau damping than the correct relativistic theory for high phase velocity electron plasma waves, e.g. those excited by Stimulated Raman Scattering [37].

Recently, Bers [38] and others [39–41] have investigated corrected relativistic theories that reduce the damping rate as observed in experiment. However, numerical evaluation and subsequent root finding for such complicated dispersion relations can be challenging. Nevertheless there has been excellent work to address various aspects of the problem. For example in [42], the authors approximate the distribution using a set of analytic basis functions combined with closed-form evaluation of the relevant integrals. In Matsuda and Smith [43], the dispersion relation for cyclotron-maser and whistler-wave instabilities is evaluated by performing a variety of manipulations to yield a smooth integration kernel but at the expense of introducing slowly decaying tails. This integrand is then treated using Gauss quadrature. In [44] the authors suggest that standard quadratures applied directly to a grid evaluated integrand could yield inaccuracies due to highly oscillatory kernels, and to avoid the problem they propose polynomial interpolation followed by analytic evaluation of the interpolant. Verscharen et. al. [45] adopt classical numerical methods, e.g. piecewise linear differencing and integration, which yields reasonable accuracy ($\sim 10^{-5}$) for their problems. Perhaps most closely related to the present work Hellinger and Trávníček observe that for weakly damped modes direct integration along the real line could be problematic. As a remedy they suggest that the contour could in principle be displaced, but they do not pursue it perhaps because for their application sufficient accuracy is obtained without it. Nevertheless, there remains open questions along the path of evaluating or solving the relevant dispersion relation over a wide range of parameters.

Simultaneously, simulation of solutions to Vlasov equations has become an important and timely topic in computational science and engineering with significant research efforts on a wide variety of techniques including semi-Lagrangian [46–49], pseudo-spectral [50–52], finite element [53, 54], finite volume [55–58], and finite difference [59–62] methods. One significant challenge in kinetic

simulation is the cost of discretization in a six dimensional phase space. As a result, many authors consider dimensionally reduced equations e.g. 2D-2P [51, 52, 63, 64], and/or high-order accurate discretizations e.g. [54, 58, 62]. Verification and benchmarking of such codes is extremely important, and while manufactured solutions can be used, the construction of exact solutions is one important aspect the present work. There exists a relatively complete analytic theory for non-relativistic Landau damping with Maxwellian equilibria which has been widely and effectively used in verification work [57, 62, 65–69]. Extension to relativistic cases appear somewhat less studied, despite the interest in relativistic kinetic simulation tools, both PIC and continuum type, e.g. [70–73]. This work seeks to close that gap.

The present manuscript explores Landau damping in the context of computational physics. First we describe a set of new mathematical techniques and computational tools that enable the evaluation and subsequent determination of roots to the kinetic dispersion relation for general equilibrium distribution functions, including for the relativistic equations. This technique enables a precise understanding of the behavior of plane wave solutions, and can therefore be considered a key part of determining exact plane-wave solutions to the linearized Vlasov-Poisson system. These tools are capable of double precision accuracy, even in very challenging regimes with very hot plasmas and relativistically correct Jüttner equilibria. The validity of these tools is then illustrated by comparison to direct continuum simulation of the Vlasov equation using the LOKI code [57, 62]. In so doing, we provide a useful benchmark for other other continuum codes by effectively providing an exact solution to the governing equations where none was previously known. Finally the tools are used to investigate highly relativistic plasmas where we show that under certain conditions the Landau root can cease to exist. Furthermore, we reveal that for certain equilibria, e.g. the Jüttner, there apparently exists superluminal modes whose phase and group velocities exceeds the speed of light. Similar results were observed in [40]. The existence of such modes may indicate that the Vlasov-Poisson system is not the physically correct model in the highly relativistic limit since it is not Lorentz invariant (for related discussion see [74]). Further study of this phenomenon, e.g. direct Vlasov simulation of driven waves and investigation of the Lorentz invariant Vlasov-Maxwell system, is outside the scope of the present work and will be taken up in follow-on investigations.

The remainder of this manuscript is organized as follows. Section 2 discusses the governing equations, and Section 3 discusses the plasma dispersion relation in a general setting. Landau damping in cold plasmas (i.e. not relativistic) is discussed in Section 4, beginning with the classical solution via special functions in Section 4.1 and then moving to our new more general approach in Section 4.2. The techniques are then extended to relativistically hot plasmas in Section 5. Verification with respect to direct kinetic simulation in a variety of dimensions and for both hot and cold plasmas is discussed in Section 6. The techniques are then applied to highly relativistic cases in Section 7, and concluding remarks given in 8. Section Appendix A discusses details about the order of integration in the new approach, and finally Appendix B discusses normalization of the Jüttner in reduced dimension settings.

2. Governing Equations

For the present study, it is sufficient to consider a kinetic description of an electron plasma with assumed immobile neutralizing ions, and self-consistent electrostatic fields. Using a continuum description with appropriate non-dimensionalization, the single-species Vlasov-Poisson system in 3 space dimensions $\mathbf{x} = [x, y, z]^T$, 3 momentum dimensions $\mathbf{p} = [p_x, p_y, p_z]^T$, and time t is expressed

$$\partial_t f + \mathbf{v} \cdot \nabla_{\mathbf{x}} f - \mathbf{E} \cdot \nabla_{\mathbf{p}} f = 0, \quad (1a)$$

$$\mathbf{E} = -\nabla\phi, \quad (1b)$$

$$\Delta\phi = 1 - \int_{\mathbf{p}} f d\mathbf{p}, \quad (1c)$$

where the integral is understood in the usual way as the definite integral over the (infinite) momentum space. In (1) ∂_t indicates the partial time derivative, $\nabla_{\mathbf{x}}$ is the vector of partial derivatives in space, $\nabla_{\mathbf{p}}$ is the vector of partial derivatives in momentum, $f(\mathbf{x}, \mathbf{p}, t)$ is the distribution function, $\mathbf{E}(\mathbf{x}, t)$ the electric field, and the relativistic velocity $\mathbf{v}(\mathbf{p}) = \gamma^{-1}\mathbf{p}$ is given using the Lorentz factor γ defined by

$$\gamma = \sqrt{1 + \frac{\|\mathbf{p}\|^2}{c^2}},$$

where $\|\cdot\|$ denotes the 2-norm and c the speed of light (units to be discussed). Note that one can also express γ in terms of \mathbf{v} as

$$\gamma = \frac{1}{\sqrt{1 - \frac{\|\mathbf{v}\|^2}{c^2}}}.$$

Note that Equation 1 is presented in dimensionless form, which has the important implication that c in Equation 1, and throughout the manuscript, is a *normalized light speed*. Therefore, $c \in (1, \infty)$ will be used as a parameter to alter the magnitude of relativistic effects with $c \rightarrow \infty$ indicating a cold non-relativistic plasma².

Assume that in physical space we seek planar waves propagating in the x -direction, with no corresponding variation in the other physical space coordinates. In this case the governing system (1) reduces

$$\partial_t f + v_x \partial_x f + \partial_x \phi \partial_{p_x} f = 0, \quad (2a)$$

$$\partial_x^2 \phi = -1 + \int_{\mathbf{p}} f d\mathbf{p}, \quad (2b)$$

which is the classical 1D Vlasov-Poisson system for fully relativistic formulation with ϕ an electric potential. Henceforth we will adopt notation indicating variation only in 1 space dimension, e.g. $f(\mathbf{x}, \mathbf{p}, t)$ will become $f(x, \mathbf{p}, t)$.

3. Developing the Plasma Dispersion Relation

To understand the nature of solutions to (2), it is useful to express the distribution as the summation of an equilibrium $f_E(\mathbf{p})$, and a perturbation $\delta f(x, \mathbf{p})$, where $f_E(\mathbf{p})$ is a momentum dependent steady state of the system with the restriction that $\int_{\mathbf{p}} f_E d\mathbf{p} = 1$. In defining f_E it is often sensible to consider the vanishing collisionality limit, and so f_E would take the form of a Maxwellian in the non-relativistic case, and a Maxwell-Jüttner in the relativistic case. However

²Although (1) is dimensionless, common physical scalings would take units of length to be the Debye length, time to be the inverse plasma frequency, and velocity to be the thermal velocity of the unperturbed distribution (i.e. the square root of the second moment of f)

the present analysis makes no such assumptions, and any time-independent distribution function would suffice. For example, one could consider plasmas which are relativistically hot in one dimension but cold in the others (essentially Maxwell-Jüttner in a single dimension and Maxwellian in others), or even distributions which are not the limit of any weakly collisional process (e.g. from experimental observation). A linearized analysis corresponds to further restricting consideration to small perturbations with $|\delta f| \ll 1$ and neglecting quadratic terms in δf to yield the linearized Vlasov-Poisson system

$$\partial_t \delta f + v_x \partial_x \delta f + \partial_x \phi \partial_{p_x} f_E = 0, \quad (3a)$$

$$\partial_x^2 \phi = \int_{\mathbf{p}} \delta f d\mathbf{p}. \quad (3b)$$

It is useful to recall the analysis in the landmark paper [11], which considers a particular x -mode characterized by wave number k (i.e. take $\delta f = \widehat{\delta f} e^{ikx}$ and $\phi = \widehat{\phi} e^{ikx}$), from whence

$$\partial_t \widehat{\delta f} + ikv_x \widehat{\delta f} + ik\widehat{\phi} \partial_{p_x} f_E = 0, \quad (4a)$$

$$-k^2 \widehat{\phi} = \int_{\mathbf{p}} \widehat{\delta f} d\mathbf{p}. \quad (4b)$$

Applying a Laplace transform with $\widetilde{\delta f} = \int_0^\infty \widehat{\delta f} e^{-st} dt$, and $\widetilde{\phi} = \int_0^\infty \widehat{\phi} e^{-st} dt$ gives

$$s\widetilde{\delta f} + ikv_x \widetilde{\delta f} + ik\widetilde{\phi} \partial_{p_x} f_E = \widetilde{\delta f}_0, \quad (5a)$$

$$-k^2 \widetilde{\phi} = \int_{\Gamma} \widetilde{\delta f} d\mathbf{p}, \quad (5b)$$

where $\widetilde{\delta f}_0$ is the initial condition, and \int_{Γ} indicates the integral over the so-called *Landau Contour*, for example as depicted in Figure 1. Integration along the Landau Contour corresponds to performing the integral over real-valued \mathbf{p} , as well as including any residue contributions from the pole located at the point $v_x = is/k$ when $\Re(s) \leq 0$. This description is at the core of our new approach to evaluation of the dispersion relation in general cases. The necessity of the Landau Contour in Equation (5b) is the core of the disagreement between Vlasov and Landau, and is described in detail in [11]. In short, the Landau Contour is required to ensure that poles in the complex s plane correctly indicate the long-time behavior upon performing the inverse Laplace transform using appropriate Bromwich contour.

Solving Equation (5a) for $\widetilde{\delta f}$, and substituting into Equation (5b) leads to

$$\widetilde{\phi} = \frac{-\int_{\Gamma} \frac{\widetilde{\delta f}_0}{s+ikv_x} d\mathbf{p}}{k^2 - ik \int_{\Gamma} \frac{\partial_{p_x} f_E}{s+ikv_x} d\mathbf{p}}. \quad (6)$$

Poles in the Laplace transformed $\widetilde{\phi}$ will indicate the long-time behavior of the electric potential, and the location of such poles is indicated by a vanishing denominator. Furthermore, to aid physical interpretation in the remainder of the manuscript, we make the choice to describe the time-behavior using temporal frequency rather than the dual Laplace transform variable s , and so make the substitution $s = -i\omega$ to give

$$D \equiv k^2 - \int_{\Gamma} \frac{\partial_{p_x} f_E}{v_x - \frac{\omega}{k}} d\mathbf{p} = 0. \quad (7)$$

D is the so-called plasma dispersion relation whose roots indicate the long-time behavior of the electric potential ϕ .

4. Landau Damping in Cold Plasmas

Evaluation of the plasma dispersion function D , and subsequent identification of roots, can be performed in closed form only in certain limited cases, e.g. a cold plasma corresponding to the weakly relativistic limit with Maxwellian equilibrium. However, for many cases of practical interest, closed-form solutions are not known, e.g. when relativistic effects become important. Nevertheless, it is useful to reiterate the known solution, and subsequently to use the cold-plasma case as a simple baseline for comparison of our new approach to evaluating D .

In the weakly relativistic limit $\gamma \rightarrow 1$, and therefore $\mathbf{p} \rightarrow \mathbf{v}$. As a result, the integrals and derivatives defining the dispersion relation can be expressed in terms of \mathbf{v} as

$$D_0 = k^2 - \int_{\Gamma} \frac{\partial_{v_x} f_M}{v_x - \frac{\omega}{k}} d\mathbf{v}, \quad (8)$$

where the notation D_0 is used to indicate the non-relativistic dispersion relation. In Equation (8), the Maxwellian equilibrium f_M , which is the equilibrium distribution in the presence of particle collisions, is explicitly indicated³. In dimensionless form this equilibrium is expressed

$$f_M(\mathbf{v}) = (2\pi)^{-\frac{3}{2}} e^{-\frac{1}{2}\|\mathbf{v}\|^2},$$

and so $\partial_{v_x} f_M = -v_x f_M$. Substituting into (8), and explicitly indicating each of the integrals leads to

$$\begin{aligned} D_0(\omega, k) &= k^2 - \int_{\Gamma} \int_{-\infty}^{\infty} \int_{-\infty}^{\infty} \frac{-v_x f_M}{v_x - \frac{\omega}{k}} dv_z dv_y dv_x, \\ &= k^2 - \int_{\Gamma} \frac{1}{\sqrt{2\pi}} \frac{-v_x e^{-\frac{1}{2}v_x^2}}{v_x - \frac{\omega}{k}} \int_{-\infty}^{\infty} \int_{-\infty}^{\infty} \frac{1}{2\pi} e^{-\frac{1}{2}(v_y^2 + v_z^2)} dv_z dv_y dv_x, \\ &= k^2 - \int_{\Gamma} \frac{1}{\sqrt{2\pi}} \frac{-v_x e^{-\frac{1}{2}v_x^2}}{v_x - \frac{\omega}{k}} dv_x, \end{aligned} \quad (9)$$

which is in agreement with [11].

4.1. The classical approach

As discussed in [75], the dispersion relation D_0 in (9) can be evaluated in closed form as

$$D_0(\omega, k) = k^2 + W\left(\frac{\omega}{k}\right), \quad (10a)$$

where

$$W(Z) = 1 + i\sqrt{\frac{\pi}{2}} Z \operatorname{erfcx}\left(\frac{Z}{\sqrt{2}}\right), \quad \operatorname{erfcx}(Z) = e^{-Z^2} \operatorname{erfc}(-iZ). \quad (10b)$$

³Electron scattering from ions involves very little energy loss but isotropizes the electron distribution on the fastest time scale. On a longer time scale electron-electron scattering leads to an isotropic Maxwell-Boltzmann distribution. Ion-ion collisions generally occur on a longer time scale and lead to an isotropic Maxwell-Boltzmann ion distribution. On yet a longer time scale, collisions lead to an equilibration of the electron and ion temperatures.

Note that Z is used throughout to denote a dummy complex variable. While useful, even these expressions present certain practical difficulties in terms of numerical evaluation. For instance, many standard math libraries do not implement error functions of complex arguments (e.g. Matlab, C/C++). Furthermore, it would be preferable to have a direct implementation of `erfcx` for complex type in order to avoid over- and under-flow issues related to the e^{-Z^2} term. For this, one can download or implement their own version, for example based on the algorithm described by Gautschi [76].

4.2. A “numerical” approach

Whatever method one uses to evaluate D_0 , the guiding principle should be that one obtains roughly machine precision in a relative sense, e.g. 16-digit accuracy for double precision. There are of course many ways to accomplish this, and here we pursue a particular approach with natural generalization to more complex cases, such as relativistically hot plasmas or non-Maxwellian equilibria.

To describe the methodology, the present discussion focuses on the evaluation of the integral term in (9), which in (10a) is identified as the W -function

$$W(Z) = - \int_{\Gamma} g_W(\xi; Z) d\xi, \quad (11a)$$

$$g_W(\xi; Z) = - \frac{1}{\sqrt{2\pi}} \frac{\xi e^{-\frac{1}{2}\xi^2}}{\xi - Z}. \quad (11b)$$

Note that $W(Z)$ is closely related to the Faddeeva (previously known as the Kramp function) Voigt, and Dawson functions for which there are well known numerical implementations [76–79].

In describing a generic and extensible approach however, it is useful to consider the Landau Contour used in evaluating (11a) in more detail. For example, Figure 1 shows the Landau Contour associated with evaluating $W(Z)$ for $Z = 1 - \frac{1}{2}i$ on the left in red, and $Z = 1 + \frac{3}{4}i$ on the right in green. The figure shows that the Landau contour lies along the real axis, but is deformed to pass

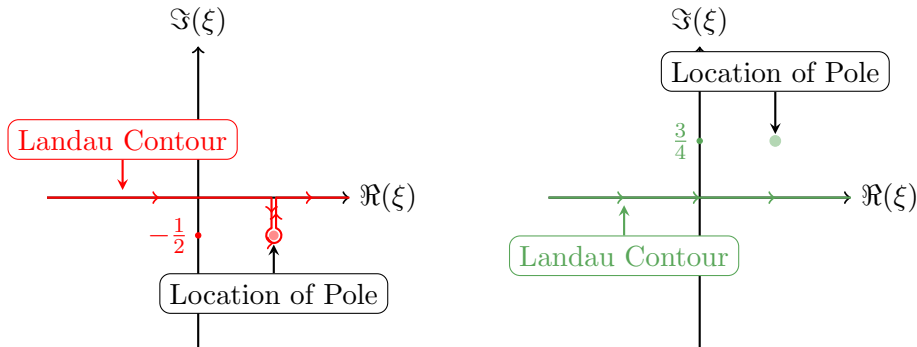


Figure 1: Representative Landau Contours for poles located below the imaginary axis (left) and above the imaginary axis (right).

below the pole whenever $\Im(Z) \leq 0$. The approach advocated here will rely on numerical quadrature to evaluate integrals to machine precision, with explicit inclusion of residues when appropriate. As such, it is useful to express the W -function as

$$W(Z) = W_I(Z) + 2\pi i W_R(Z), \quad (12a)$$

where

$$W_I(Z) = - \int_{-\infty}^{\infty} g_W(\xi; Z) d\xi, \quad (12b)$$

$$W_R(Z) = \begin{cases} (2\pi)^{-\frac{1}{2}} Z e^{-\frac{1}{2}Z^2} & \Im(Z) < 0 \\ \frac{1}{2}(2\pi)^{-\frac{1}{2}} Z e^{-\frac{1}{2}Z^2} & \Im(Z) = 0 \\ 0 & \text{else.} \end{cases} \quad (12c)$$

Here W_I indicates the integral portion of W , while W_R indicates any residue contributions from poles when $\Im(Z) \leq 0$. Note that the difference between the cases with $\Im(Z) < 0$ and $\Im(Z) = 0$ is due to the contour being circular for the former but semi-circular in the latter case.

4.2.1. Quadrature evaluation of W_I

To evaluate $W_I(Z)$ for $\Im(Z) \neq 0$ in the form suggested by Equation (12), numerical quadrature can be employed⁴. Importantly if $\Im(Z) \neq 0$, the integrand g_W is a C^∞ function with exponentially decaying tails for $\Re(\xi) \rightarrow \pm\infty$. Therefore, as discussed in [80], trapezoidal quadrature is exponentially convergent in the sense that it converges faster than $\mathcal{O}\left(\frac{1}{N^p}\right)$ for any finite p with N the number of quadrature points. Note that if the integrand is not continuous or lacks sufficient smoothness, the present approach is not applicable and would need to be extended, e.g. by using difference approximation of the derivative or perhaps by combination with ideas from [42, 43, 81] for example. Even in the case where the integrand is smooth, some care must be taken in using trapezoidal quadrature, e.g. the integration bounds must be taken sufficiently large that further expanding them does not change the computed integral approximation in the given computer number system, see [80]. Therefore, it is useful to precisely define the approximation and introduce notation. Consider the function $h(x)$, the trapezoidal approximation to the integral is defined

$${}^\beta_\alpha T_N(h(\xi)) \approx \int_{\xi=\alpha}^{\beta} h(\xi) d\xi, \quad (13a)$$

where

$${}^\beta_\alpha T_N(h(\xi)) = \frac{\beta - \alpha}{N} \sum_{j=0}^{N-1} \frac{h(\xi_j) + h(\xi_{j+1})}{2}, \quad (13b)$$

with $\xi_j = \alpha + \frac{\beta - \alpha}{N} j$.

4.2.2. Displacing the integration contour

On some level the fact that trapezoidal quadrature is exponentially convergent means it is an excellent choice that will yield accurate results using “reasonable” numbers of quadrature points N (note that the term “accurate” will be used throughout this manuscript to indicate machine precision). However, practical cases of interest often include $\Im(Z) \approx 0$, in which case the behavior of g_W can include both coarse and fine scale features due to the close proximity of the pole to the integration contour. This scenario can lead to large and expensive quadratures for accurate integration. Fortunately however, the contour can be moved or deformed, essentially at will, in

⁴The case of $\Im(Z) = 0$ would need special treatment, but the subsequent discussion in the manuscript covers this too.

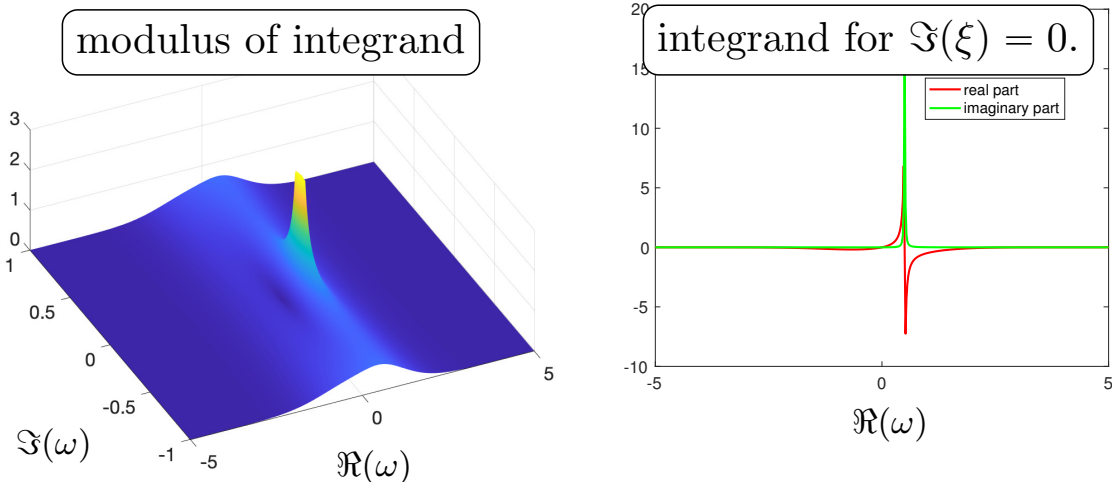


Figure 2: At left is $\min(|g_W(\xi; Z_0)|, 3)$ for $Z = Z_0 = \frac{1}{2} - \frac{1}{100}i$ and complex ξ . Here the cap of 3 ensures that variation away from the pole, whose location is clearly seen, can still be observed. At right are the real and imaginary parts of the integrand $g_W(\xi, Z_0)$, i.e. for $\Im(\xi) = 0$.

the complex plane as long as the deforming contour does not cross any poles or branch cuts of the integrand. For example for $\Im(Z) < 0$ and any $\eta > 0$, W_I can be expressed

$$W_I(Z) = - \int_{-\infty}^{\infty} \tilde{g}_W(\xi; Z, \eta) d\xi \quad (14a)$$

where

$$\tilde{g}_W(\xi; Z, \eta) = (2\pi)^{-\frac{1}{2}} \frac{-(\xi + i\eta)e^{-\frac{\xi^2}{2} - i\xi\eta + \frac{\eta^2}{2}}}{\xi + i\eta - Z}. \quad (14b)$$

In fact, as will be used later in this document, the contour can be moved across poles as well, provided the residue of the pole is appropriately accounted for. Furthermore, although not pursued here, more complicated deformations could be considered.

As an example, consider $Z_0 = \frac{1}{2} - \frac{1}{100}i$. The left panel of Figure 2 shows the modulus of the integrand as a function of complex ξ and a cap of 3 so that the behavior of the pole doesn't swamp all other features, i.e. $\min(|g_W(\xi; Z_0)|, 3)$. The location of the pole is clear, and its proximity to the integration contour with $\Im(\xi) = 0$ will clearly have significant effect on the behavior of the integrand. To more clearly understand this effect, the right panel of Figure 2 shows the real and imaginary parts of the integrand $g_W(\xi, Z_0)$ for $\Im(\xi) = 0$. Even though these curves are in fact smooth, i.e. C^∞ , accurate quadrature for this function would require exceedingly large numbers of quadrature points due to combination of slowly varying large scale oscillations and rapid variation near $\xi = \frac{1}{2}$. Quantitative estimates of this cost is presented in Figure 4.

On the other hand, displacing the line of integration away from the pole may change the nature of the integrand and ultimately the nature of the quadrature required for machine precision. Appealing to Equation (14b), which describes the integrand as a function of vertical displacement η , one can observe that displacement away from the pole will tend to mollify its influence, and thereby enable accurate integration with smaller quadratures. To illustrate this effect, Figure 3 shows the real and imaginary parts of $\tilde{g}_W(\xi; Z_0, 1)$ and $\tilde{g}_W(\xi; Z_0, 5)$, i.e. the line of integration

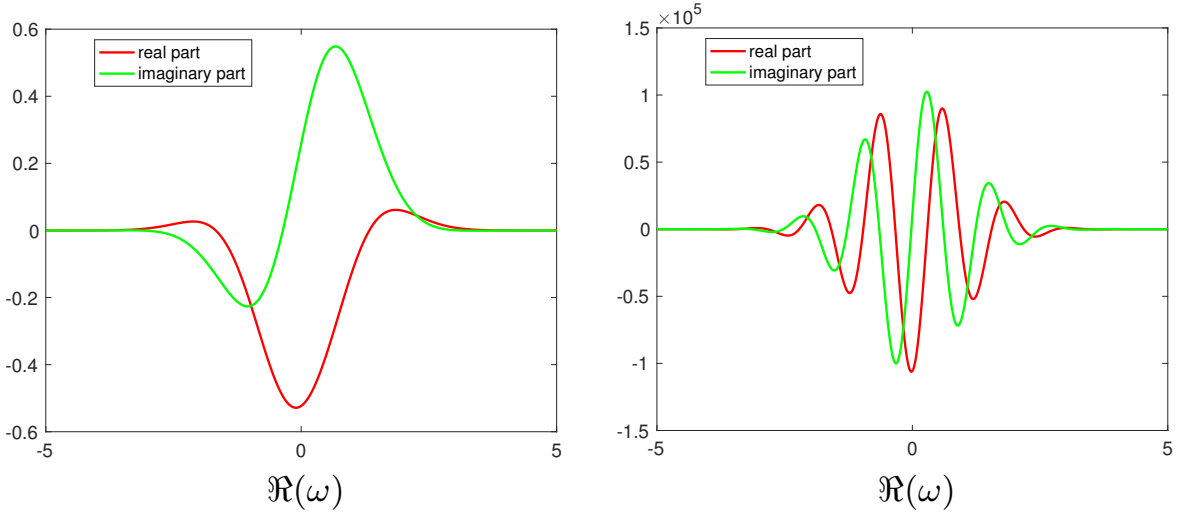
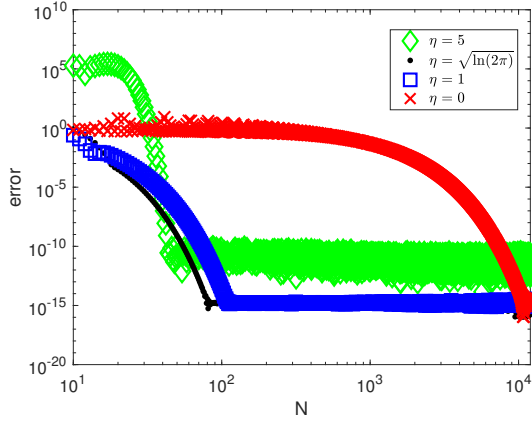


Figure 3: Real and imaginary parts of $\tilde{g}_W(\xi; Z_0, 1)$ (left) and $\tilde{g}_W(\xi; Z_0, 5)$ (right). These are line of integration shifted vertically by 1 or 5 respectively.

vertically shifted by 1 or 5 respectively. These plots reveal two primary features: Firstly, as the line of integration is moved away from the pole and into the upper half plane, the magnitude of the smallest scales tend to decrease, which would imply that accurate quadratures require fewer points. Secondly, the magnitude of the real and imaginary parts of the integrand tends to grow exponentially as $\Im(\xi) \rightarrow \infty$, which tends to make the condition of the problem progressively worse.

From the perspective of numerical quadrature, the fact that small-scale features tend to decay as $\eta \rightarrow \pm\infty$ leads one to desire large η . On the other hand, because integrand becomes large in magnitude as $\eta \rightarrow \infty$, the condition of the definite integral also increases, which leads one to desire small η . To probe the interplay of these two competing demands in the context of the present example with $Z = Z_0$, the left panel of Figure 4 shows the error in ${}_{-10}^{10}T_N(-\tilde{g}_W(\xi; Z_0, \eta))$ for various values of η , which are approximations to $W_I(Z_0)$ as defined in Equation (14a). For reference, $W_I(Z_0) \approx -0.76159 + 0.54465i$. In the figure one observes exponential convergence of the quadrature approximation since the errors in log-log scaling are concave downward prior to numerical saturation (here in double precision). Also, in accordance with expectation, one observes that the number of points required for error saturation appears to be decreasing as η increases. The appearance of results for $\eta = \sqrt{\ln(2\pi)}$ may seem a mystery, but will be discussed momentarily. Finally, the magnitude of the error at numerical saturation is generally increasing with η for large η , but for small η the picture is potentially nuanced (particularly for cases where the pole is exceedingly close to the contour and so the quadrature will necessarily include large and small values). These observations about error saturation are summarized in the table on the right of Figure 4 which shows the number of quadrature points required for error saturation in double precision, N_ϵ , and the approximate error at saturation, E_ϵ , as functions of the offset η .

The question of how to pick η centers on minimizing, or at least reducing, the number of quadrature points, while avoiding ill-conditioning in the integral formulation. Although it is not a focus of the present manuscript, keeping the number of quadrature points low can be important in order to keep the computational cost in check. For example in [82, 83], fluid modeling of stimulated scattering uses a large number of dispersion relation calculations, and so overly costly calls could



Quad points and error at saturation		
η	N_ϵ (approx)	E_ϵ (approx)
0	$\approx 10,000$	2.5×10^{-15}
1	110	2.0×10^{-15}
$\sqrt{\ln(2\pi)}$	80	1.5×10^{-15}
5	45	2×10^{-11}

Figure 4: At left are the errors in the N -point trapezoidal quadrature approximation to $W_I(Z_0) \approx {}_{-10}T_N(-\tilde{g}_W(\xi; Z_0, \eta))$. Here the vertical offset is given by η (see the figure legend). At right is the number of quadrature points required for error saturation in double precision, N_ϵ , and the approximate error at saturation, E_ϵ for the various η .

add up. A brief discussion of cost with respect to Gautschi's algorithm is given in Section 4.3. As seen in Figure 4, the minimum number required to attain saturation depends on the proximity of the contour to the pole, but taking marginally too many quadrature points is not generally detrimental to the result (although at extra unnecessary cost). On the other hand, taking too large an offset will yield unacceptable loss in accuracy due to ill-conditioning. Therefore our choice will be based on using a reasonably small fixed number of quadrature points (e.g. 200 for double precision), and determining η based on arguments about conditioning. Using a fixed number of quadrature points implies that the contour should be displaced at least some distance from the pole for accurate integration, call that distance δ . Because we wish to limit the growth of the condition number, the direction of displacement should be dictated by $\Im(Z)$, i.e. if the pole is above or below the imaginary axis. Specifically, $\Im(Z) \leq 0$ implies $\eta \geq 0$, while $\Im(Z) > 0$ implies $\eta \leq 0$. In either case, the relative growth in the magnitude of the integrand (14b) can be bounded by the case $\eta = 0$, where limiting the exponentially growing factor in Equation (14b) to be less than unity yields the threshold value $\delta = \sqrt{\ln(2\pi)}$.

4.2.3. Evaluation the W -function

With the basic concepts in place, the complete approach to evaluation of $W(z)$ is now given by

$$W(Z) \approx \begin{cases} \xi_+ T_N(-\tilde{g}_W(\xi; Z, \eta_+)) + 2\pi i W_R(Z) & \Im(Z) \leq 0 \\ \xi_- T_N(-\tilde{g}_W(\xi; Z, \eta_-)) & \text{else,} \end{cases} \quad (15a)$$

where,

$$\eta_+ = \max(\Im(Z) + \delta, 0) \quad (15b)$$

$$\eta_- = \min(\Im(Z) - \delta, 0). \quad (15c)$$

One interesting aspect of the present formulation is that, by construction, the line integral is chosen to avoid any poles. As a result, deviations around poles for the Landau contour are all circular, and there are not separate cases for $\Im(Z) < 0$ and $\Im(Z) = 0$, as was the case in (12) where the

pole was on the line integral when $\Im(Z) = 0$. For double precision accuracy it is sufficient to take $\xi_- = -10$, $\xi_+ = 10$, and $N = 200$. To understand the formulation in Equation (15) in terms of the implied integration contours, it will suffice to describe the case $\Im(Z) \leq 0$ since the case with $\Im(Z) > 0$ follows similarly. Therefore, Figure 5 presents the implied contours for evaluating $W(Z)$ for $Z = 1 - \frac{1}{2}i$ and $Z = 1 - \frac{3}{2}i$ as formulated in Equation (15). For the case with $Z = 1 - \frac{1}{2}i$, the pole is sufficiently close to the axis so that ensuring the integration contour is no closer than d to the pole places the line of integration in the upper half plane. Therefore the offset value is $\eta = \Im(Z) + \delta$. On the other hand for the case $Z = 1 - \frac{3}{2}i$, the pole is well below the axis and integration with $\eta = 0$ is sufficient to separate.

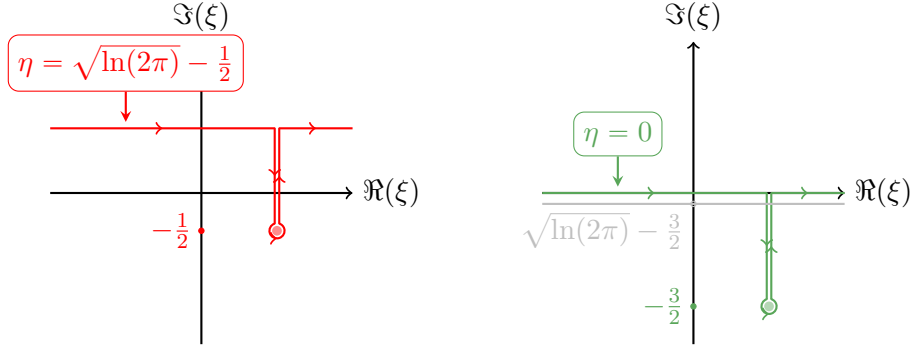


Figure 5: Integration contour for a pole below the real axis, the left being close to the axis and the right being sufficiently far from the real axis that the Landau Contour is used.

4.3. Comparison to Gautschi's algorithm

Having described a new approach to evaluate the W -function, we return to the full plasma dispersion function for the cold plasma case, D_0 as given in Equation (8), and provide a comparison to the exact result to full numerical precision, as well as an existing algorithms which is typical of those employed in practice. To obtain a full double precision result, D_0 is evaluated as in Equation (10a) in Maple using 50 digit arithmetic, and the result is then truncated to 16 digits. As an example of existing functionality, Gautschi's algorithm is used to evaluate erfcx with parameters selected for double precision [76] (i.e. in the notation used by Gautschi in [76] $x_0 = 8.72$, $y_0 = 10.06$ $h_0 = 2$, $n_0 = 6$, $n_1 = 40$, $\nu_0 = 9$, and $\nu_1 = 39$). On the other hand, the new quadrature approach with displaced contour uses $\xi_- = -10$, $\xi_+ = 10$, and $N = 200$. Figure 6 shows results for $k = \frac{1}{3}$ with $\Re(\omega) \in [0, 2]$ and $\Im(\omega) \in [-2, 1]$. In all cases the plots use 400 uniformly distributed points in the real axis, and 402 uniformly distributed points in the imaginary axis. At the top of the figure are visualizations of the dispersion function itself with the left showing the zero contours of the real and imaginary parts, while the complex argument is shown at right. The bottom portion of the figure shows the relative error in the evaluations with respect to the exact solution to full double precision accuracy. The plots are expressed in terms of the number of correct significant figures calculated as

$$\text{Digits}(\omega) = -\max\left(\log_{10}\left(\frac{|D_0(\omega) - \tilde{D}_0(\omega)|}{|D_0(\omega)|}\right), -17\right),$$

where $D_0(\omega)$ indicates the exact result, and $\tilde{D}_0(\omega)$ indicates the computed result with either the Gautschi algorithm or numerical quadrature. The cap of 17 digits is simple due to the fact that in some cases the computed result is exact to all represented digits, a situation which would lead

to plotting irregularities. The plots make clear that the Gautschi-based algorithm is comparable to the quadrature-based algorithm with both yielding 13-17 digits of accuracy for all cases. In fact the quadrature-based algorithm is slightly more reliable in producing full double precision accuracy with 16-17 digits. In addition, it is be useful to report the relative cost of evaluation of the dispersion relation as used to produce the plots in Figure 6. Both the Gautschi algorithm and the new quadrature approach are implemented here in MATLAB and not highly optimized, and so caution in interpreting performance numbers is warranted. In both cases there is no use of vectorization and so timings essentially represent the cost to make 160,800 calls to the respective dispersion relation function. A representative run on a MacBook Pro laptop with Apple M2 Max processor has the Gautschi algorithm requiring 1.15 seconds, the quadrature approach requiring 1.12 seconds, and so the quadrature algorithm is roughly 3% more efficient than the Gautschi-based one.

A further check of the accuracy in the various implementations is the evaluation of the Landau root. Recall that the Landau root, ω_L , corresponds to the the least damped mode in the system, and so for sufficiently long times will indicate the observed linear frequency and decay rate for a freely propagating plane Langmuir wave. Therefore, the Landau root is an important quantity with physical significance. For reference, the root is computed in Maple using Newton's method with 50 digit arithmetic and a very small tolerance. The result is then rounded to 16 digits and therefore represents the exact Landau root to 16 digits. Similar computations are carried out using the quadrature and Gautschi implementations⁵. Results for these three methods are

$$\omega_{L,\text{exact}} = 1.200108902115360 - 0.025873679887016i \quad (16a)$$

$$\omega_{L,\text{Gautschi}} = 1.200108902115361 - 0.025873679887016i \quad (16b)$$

$$\omega_{L,\text{quadrature}} = 1.200108902115360 - 0.025873679887016i, \quad (16c)$$

which shows that the new quadrature-based algorithm gives the exact result to 16 digits, while the Gautschi-based algorithm differs only in the 16th digit.

5. Landau damping in relativistically hot plasmas

Unfortunately there is no known closed-form evaluation of the plasma dispersion function in Equation (7) for hot plasmas where relativistic effects are important. However, the quadrature-based approach outlined in Section 4 is naturally extensible to this regime and represents a viable path to evaluating the dispersion relation and ultimately determining roots of the same. To describe this extension, Section 5.1 begins in the relativistic limit but with a Maxwellian equilibria in momentum space. This case contains all the essential features of the more physically relevant Maxwell-Jüttner equilibria, but is somewhat simpler to describe. Then in Section 5.2 the algorithm is discussed in the context of the Maxwell-Jüttner equilibria.

5.1. Maxwellian equilibria function in a hot plasma

As a simple starting point to describe quadrature-based evaluation of the dispersion relation in a relativistically hot plasma, consider the Maxwellian equilibrium distribution in momentum space

$$f_M(\mathbf{p}) = (2\pi)^{-\frac{3}{2}} e^{-\frac{1}{2}\|\mathbf{p}\|^2}. \quad (17)$$

⁵Note that implementation of Newton's method of course requires $\frac{dD_0}{d\omega}$, which is straightforward.

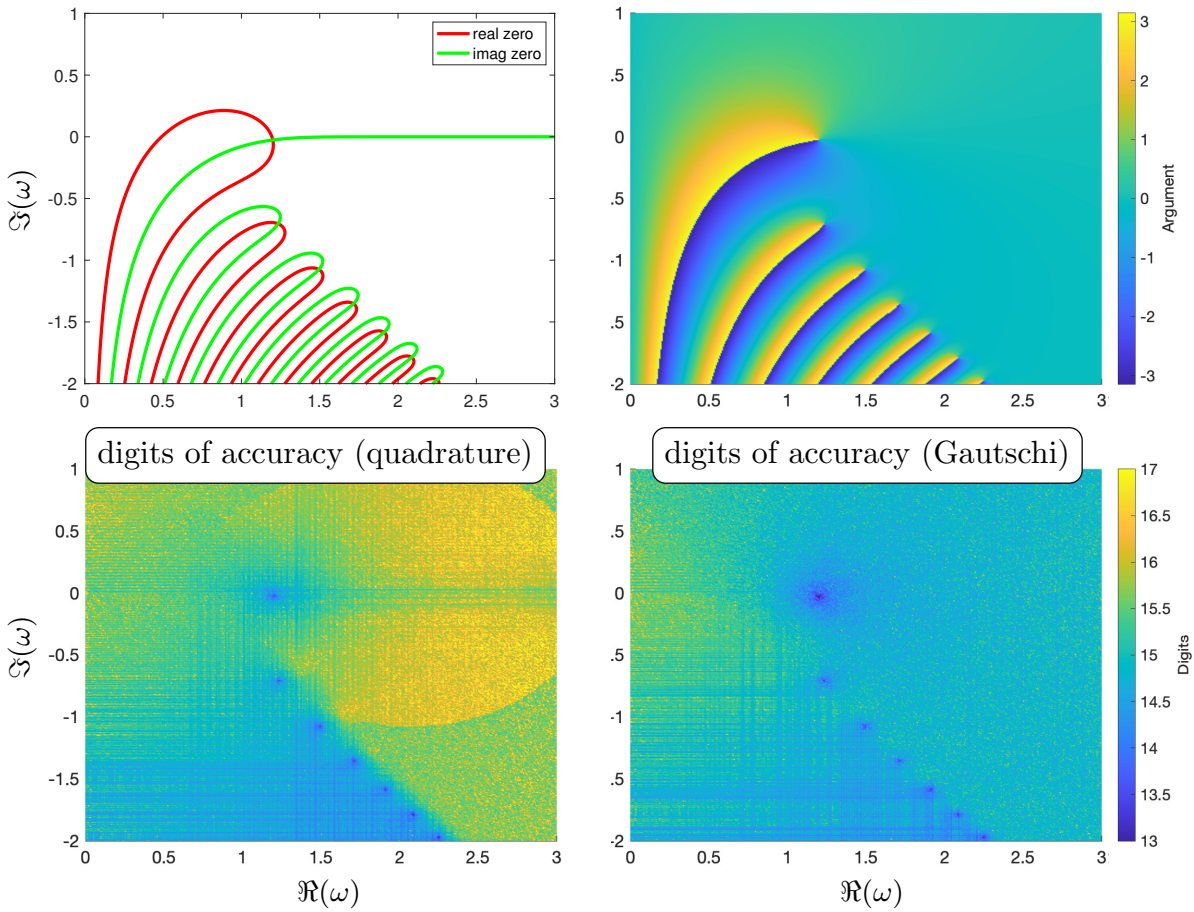


Figure 6: At the top are visualizations of the dispersion function $D_0(\omega)$ with the left showing the zero contours of the real and imaginary parts, while the complex argument is shown at right. At bottom are plots showing the number of correct significant figures in the results as computed by the quadrature approach at left, and Gautschi's algorithm at right.

Substituting Equation (17) into (7) and expanding the integrals gives

$$D_c^M(\omega, k) = k^2 - \int_{-\infty}^{\infty} \int_{-\infty}^{\infty} \int_{\Gamma} \frac{-p_x f_M(\mathbf{p})}{v_x(\mathbf{p}) - \frac{\omega}{k}} dp_x dp_y dp_z, \quad (18a)$$

where c is the normalized velocity of light and M indicates a Maxwellian equilibria and

$$v_x(\mathbf{p}) = \frac{p_x}{\sqrt{1 + \frac{\|\mathbf{p}\|^2}{c^2}}}. \quad (18b)$$

Note that throughout this work, the definition of the square root is the usual one where the branch cut lies along the negative real axis, i.e. for $Z = r e^{i\theta}$ where $r \geq 0$ and $\theta \in [-\pi, \pi]$, then $\sqrt{Z} = \sqrt{r} e^{i\frac{\theta}{2}}$ with \sqrt{r} being the principle root.

5.1.1. Quadrature Evaluation for Maxwellian

Perhaps the most significant practical difference from the cold (non-relativistic) case is the fact that, due to the functional form of the dependence of v_x on \mathbf{p} in (18b), the integrand no longer has a tensor product structure. As a result, the multi-dimensional integral cannot be factored into the products of single dimensional integrals, and must therefore be performed using multidimensional quadrature. Furthermore, the integrand now has both a pole, and branch points with corresponding branch cuts. To describe the quadrature-based approach to evaluating the dispersion function, Equation (18a) is expressed as

$$D_c^M(\omega, k) = k^2 - \int_{-\infty}^{\infty} \int_{-\infty}^{\infty} W_c^M\left(\frac{\omega}{k}, \mathbf{p}_{\perp}\right) d\mathbf{p}_{\perp}, \quad (19a)$$

where $\mathbf{p}_{\perp} = [p_y, p_z]^T \in \Re^2$ so that $p_y^2 + p_z^2 = \|\mathbf{p}_{\perp}\|^2$ and

$$W_c^M(Z, \mathbf{p}_{\perp}) = \int_{\Gamma} g_c^M(\xi_x; Z, \mathbf{p}_{\perp}) d\xi_x, \quad (19b)$$

$$g_c^M(\xi_x; Z, \mathbf{p}_{\perp}) = (2\pi)^{-\frac{3}{2}} \frac{-\xi_x e^{-\frac{1}{2}(\xi_x^2 + \|\mathbf{p}_{\perp}\|^2)}}{\frac{c\xi_x}{\sqrt{c^2 + \xi_x^2 + \|\mathbf{p}_{\perp}\|^2}} - Z}. \quad (19c)$$

The notation, W_c^M , adopted in Equation (19) is chosen to illustrate a correspondence to the W -function in (10b), but here with c being the normalized velocity of light and M indicating a Maxwellian equilibria. Similar notation is used to define the integrand g_c^M , where, in addition, the dependence on \mathbf{p}_{\perp} is made explicit, and the dummy variable ξ_x is used as a way to indicate that the present integral originates from p_x integration. Because it will be useful in the discussion to follow, the location of the pole in g_c^M will be indicated as $\bar{\xi}_x$, where

$$\bar{\xi}_x = \sqrt{\frac{Z^2(c^2 + \|\mathbf{p}_{\perp}\|^2)}{c^2 - Z^2}}, \quad (20)$$

and we again recall that the square root is the usual one with branch cut along the negative real axis. Furthermore, in the complex ξ_x plane, g_c^M has branch points at $\xi_x = \pm i\sqrt{c^2 + \|\mathbf{p}_{\perp}\|^2}$, with branch cuts extending outward along the imaginary axis extending to $\pm i\infty$ respectively. Importantly, this implies that there are no branch cuts in the region where $|\Im(\xi_x)| < c$ for any \mathbf{p}_{\perp} .

Similar to the cold plasma case, W_c^M can be represented in terms of its integral and residue portions as

$$W_c^M(Z, \mathbf{p}_\perp) = (W_c^M)_I(Z, \mathbf{p}_\perp) + 2\pi i (W_c^M)_R(Z, \mathbf{p}_\perp), \quad (21a)$$

with

$$(W_c^M)_I(Z, \mathbf{p}_\perp) = \int_{-\infty}^{\infty} g_c^M(\xi_x; Z, \mathbf{p}_\perp) d\xi_x, \quad (21b)$$

$$(W_c^M)_R(Z, \mathbf{p}_\perp) = \begin{cases} (2\pi)^{-\frac{3}{2}} \frac{\bar{\xi}_x e^{-\frac{1}{2}(\bar{\xi}_x^2 + \|\mathbf{p}_\perp\|^2)}}{Q'(\bar{\xi}_x; \mathbf{p}_\perp)} & \Im(\bar{\xi}_x) < 0 \\ \frac{1}{2}(2\pi)^{-\frac{3}{2}} \frac{\bar{\xi}_x e^{-\frac{1}{2}(\bar{\xi}_x^2 + \|\mathbf{p}_\perp\|^2)}}{Q'(\bar{\xi}_x; \mathbf{p}_\perp)} & \Im(\bar{\xi}_x) = 0 \\ 0 & \text{else.} \end{cases} \quad (21c)$$

Here, Q' is the ξ -derivative of the denominator of the integrand, i.e.

$$Q(\bar{\xi}_x; \mathbf{p}_\perp) = \frac{c\bar{\xi}_x}{\sqrt{c^2 + \bar{\xi}_x^2 + \|\mathbf{p}_\perp\|^2}} - Z, \quad (22a)$$

$$Q'(\bar{\xi}_x; \mathbf{p}_\perp) = c \frac{c^2 + \|\mathbf{p}_\perp\|^2}{(c^2 + \bar{\xi}_x^2 + \|\mathbf{p}_\perp\|^2)^{\frac{3}{2}}}. \quad (22b)$$

While the residue portion of W_c^M in (21c) can be easily evaluated in closed form, the integral portion in (21b) cannot. However, straightforward extension of the basic quadrature approach used to evaluate the W -function, as described in Section 4.2.3, gives a practical way to obtain machine precision. For example for $\Im(\bar{\xi}_x) \leq 0$ and any $\eta \in [0, c)$, $(W_c^M)_I$ can be expressed

$$(W_c^M)_I(Z, \mathbf{p}_\perp) = \int_{-\infty}^{\infty} \widetilde{g}_c^M(\xi_x; Z, \mathbf{p}_\perp, \eta) d\xi_x \quad (23a)$$

where

$$\widetilde{g}_c^M(\xi_x; Z, \mathbf{p}_\perp, \eta) \equiv (2\pi)^{-\frac{3}{2}} \frac{-(\xi_x + i\eta)e^{-\frac{1}{2}((\xi_x + i\eta)^2 + \|\mathbf{p}_\perp\|^2)}}{\frac{c(\xi_x + i\eta)}{\sqrt{c^2 + (\xi_x + i\eta)^2 + \|\mathbf{p}_\perp\|^2}} - Z}. \quad (23b)$$

This represents a simple vertical shift of the line of integration away from the real axis in order to facilitate a machine precision accurate quadrature using a reasonable number of quadrature points, as previously discussed. Note however, that the restriction $\eta \in [0, c)$, which is a simple way to avoid displacing the contour past branch points for all \mathbf{p}_\perp , puts certain limitations on how hot (i.e. how relativistic) the plasma can become and still employ this simple shift. Using the suggestion outlined in this manuscript, the limiting value is given by $c \approx \sqrt{\ln(2\pi)} \approx 1.36$. Note however that we experience no difficulties even as far as $c = 1.5$ which are the hottest plasmas considered in the present work. A similar shift of the line of integration downward is pursued when $\Im(\bar{\xi}_x) > 0$. Using these shifted contours, along with the exponentially accurate trapezoidal quadrature with N points, the evaluation of W_c^M becomes

$$W_c^M(Z, \mathbf{p}_\perp) \approx \begin{cases} \int_{\xi_{x-}}^{\xi_{x+}} T_{N_x}(-\widetilde{g}_c^M(\xi_x; z, \mathbf{p}_\perp, \eta_+)) + 2\pi i (W_c^M)_R(Z, \mathbf{p}_\perp) & \Im(Z) \leq 0 \\ \int_{\xi_{x-}}^{\xi_{x+}} T_{N_x}(-\widetilde{g}_c^M(\xi_x; Z, \mathbf{p}_\perp, \eta_-)) & \text{else,} \end{cases} \quad (24a)$$

where,

$$\eta_+ = \max(\Im(Z) + \delta, 0) \quad (24b)$$

$$\eta_- = \min(\Im(Z) - \delta, 0). \quad (24c)$$

As before, in this formulation there are not separate cases for $\Im(Z) < 0$ and $\Im(Z) = 0$ because the line of integration is specifically chosen to avoid poles. Also as before, $\delta = \sqrt{\ln(2\pi)}$. For double precision accuracy it is sufficient to take $\xi_{x\pm} = \pm 10$, and the number of quadrature points to be $N_x = 200$.

Finally, to evaluate the full dispersion function in (19), the exponentially accurate trapezoidal quadrature is also employed in the \mathbf{p}_\perp directions to give

$$D_c^M(\omega, k) \approx k^2 - \frac{\xi_{z+} T_{N_z}}{\xi_{z-} T_{N_z}} \left[\frac{\xi_{y+} T_{N_y}}{\xi_{y-} T_{N_y}} \left(W_c^M \left(\frac{\omega}{k}, [\xi_y, \xi_z] \right) \right) \right], \quad (25)$$

where W_c^M is given by (24) and the quadratures are understood to take place over ξ_y and ξ_z respectively. For double precision accuracy it is again sufficient to take $\xi_{y\pm} = \xi_{z\pm} = \pm 10$, and $N_y = N_z = 200$. Finally, note that numerical integration must be taken over the Landau contour in the p_x -space first to account for any contribution from the pole at $\bar{\xi}_x$. The order of the remaining quadratures is irrelevant. Further discussion on this matter is relegated to Appendix A.

5.1.2. Sample Results for Maxwellian Equilibrium

Application of the the formulation in (25) is used to evaluate the dispersion function for plasmas with varying degrees of relativistic effects. For example, Figure 7 shows the real and imaginary zero contours for $k = 1/3$ with $c = 8$ (strongly relativistic) and $c = 20$ (weakly relativistic). For comparison, zero contours for the nonrelativistic case are presented in Figure 6. As has been observed elsewhere in the literature [40], the spectrum of roots is seen to form a ‘‘hook’’ which terminates on the real axis at $\omega = ck$. Thus there formally exists roots of the dispersion relation with arbitrarily small damping, but with phase velocity approaching the speed of light.

More relevant to physical systems would be roots with smaller $|\omega|$, the smallest of which is identified here as the ‘‘Landau root’’⁶. As before, Newton’s method can be employed to compute this root, which is listed in Table 1. Also in Table 1 are computed Landau roots for dimensionally reduced Vlasov systems, i.e. Landau roots for 1-, 2-, and 3-momentum dimension (1P, 2P, and 3P respectively) Vlasov systems. This is important because, due to the high cost of kinetic simulation, many practitioners have 1P and 2P codes, and providing these additional benchmarks gives a useful metric by which to measure code performance. Extension of the methodology to compute these roots is straightforward, and involves posing the problem in the reduced dimensionality momentum space with appropriate normalization of the Maxwellian as $f_M^{(d)}(\mathbf{p}) = (2\pi)^{-\frac{d}{2}} e^{-\frac{1}{2}\|\mathbf{p}\|^2}$ where d indicates the dimensionality. Integrals are then simply taken in the existent dimensionality. Note that in the nonrelativistic case, dimensional reduction does not alter the result. Also note that another way to interpret reduced dimensionality systems is to consider the 3P equations but for a distribution that is anisotropically hot in only 1 or 2 directions.

5.2. Maxwell-Jüttner equilibria function in a hot plasma

Often when one is interested in relativistically hot plasmas, the relevant equilibrium distribution is the relativistic Maxwell-Jüttner, since it is the steady distribution for collisional plasmas in this

⁶Note that generally the Landau root is identified as the root with smallest damping, but in the relativistic case this distinction becomes tricky due to the presence of weakly damped roots near $\omega = ck$.

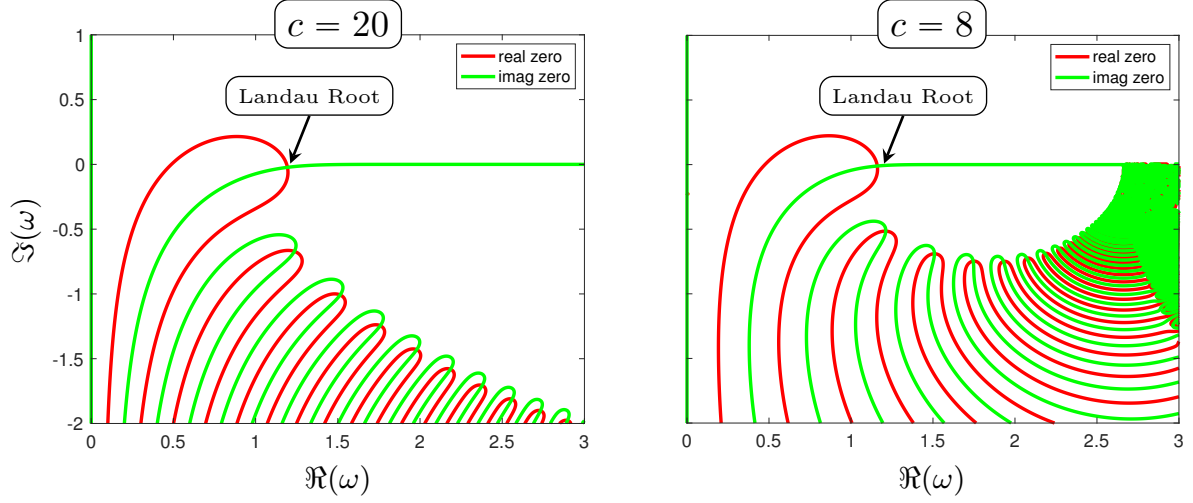


Figure 7: Zero contours of the real and imaginary parts of the relativistic dispersion relation with Maxwellian equilibrium for $c = 20$ (left) and $c = 8$ (right). Recall that for the scaling employed here $c = 8$ is more relativistic (i.e. hotter) than $c = 20$. The spectrum of roots is seen to form a hook which terminates on the real axis at $\omega = ck$. The location of the Landau root is also indicated, with the exact values listed in Table 1.

Maxwellian		
	$c = 20$	$c = 8$
$d = 1$	$1.1955073 - i0.02307958$	$1.1712408 - i0.01133209$
$d = 2$	$1.1945206 - i0.02298272$	$1.1657767 - i0.01113948$
$d = 3$	$1.1935373 - i0.02288638$	$1.1604138 - i0.01094865$

Table 1: Table of Landau roots for Maxwellian equilibrium in various momentum-space dimensions given by d with $c = 20$ (weakly relativistic) and $c = 8$ (strongly relativistic).

regime. In the present work the Jüttner is expressed

$$f_J(\mathbf{p}) = A_J e^{c^2(1-\gamma)}, \quad (26a)$$

where A_J is the normalizing constant to assure the equilibrium satisfies the restriction $\int_{\mathbf{p}} f_E d\mathbf{p} = 1$. Following the discussion in [84, 85], A_J is

$$A_J = \frac{1}{4\pi c e^{c^2} K_2(c^2)}, \quad (26b)$$

where K_ν is the modified Bessel function of the second kind of order ν . Note that in (26) there appears to be an unnecessary repetition of a factor of e^{c^2} in the denominator of A_J and then as a multiplier in the exponential. This seemingly strange formulation is numerically important because it ensures that $A_J = O(1)$ and $c^2(1-\gamma) = O(-\frac{c^2}{2})$ as $c \rightarrow \infty$, which avoids potentially problematic over or underflows for even moderately large c . However the explicit inclusion of e^{c^2} into A_J introduces its own source of numerical overflow for $c \gtrsim 25$. This difficulty is easily avoided by introducing a series expansion for A_J about $c = \infty$ for sufficiently large c . In this work, full double precision accuracy is obtained with A_J represented as

$$A_J = \begin{cases} \frac{1}{4\pi c e^{c^2} K_2(c^2)} & \text{if } |c| < 10 \\ (2\pi)^{-\frac{3}{2}} E & \text{else} \end{cases} \quad (27a)$$

where

$$E = 1 - \frac{15}{8c^2} + \frac{345}{128c^4} - \frac{3285}{1024c^6} + \frac{95355}{32768c^8} - \frac{232065}{262144c^{10}} - \frac{19559475}{4194304c^{12}} + \frac{602889075}{33554432c^{14}} - \frac{110788764525}{2147483648c^{16}} + \frac{2598854647275}{17179869184c^{18}} + \mathcal{O}(c^{-20}). \quad (27b)$$

Note that for dimensionally reduced equations (e.g. the Jüttner in 1D or 2D), normalization is discussed in Appendix B.

5.2.1. Quadrature Evaluation for Maxwell-Jüttner Equilibrium

As before, the relativistic dispersion function will be evaluated to machine precision using quadrature. Therefore, the dispersion function is represented as

$$D_c^J(\omega, k) = k^2 - \int_{-\infty}^{\infty} \int_{-\infty}^{\infty} W_c^J\left(\frac{\omega}{k}, \mathbf{p}_\perp\right) d\mathbf{p}_\perp, \quad (28a)$$

$$W_c^J(Z, \mathbf{p}_\perp) = \int_{\Gamma} g_c^J(\xi_x; Z, \mathbf{p}_\perp) d\xi_x \quad (28b)$$

$$g_c^J(\xi_x; Z, \mathbf{p}_\perp) = A_J \frac{-\xi_x e^{c^2(1-\tilde{\gamma})}}{\xi_x - Z\tilde{\gamma}} \quad (28c)$$

$$\tilde{\gamma} \equiv \sqrt{1 + \frac{\xi_x^2 + \|\mathbf{p}_\perp\|^2}{c^2}}. \quad (28d)$$

Much of the remaining formulation follows similar lines as for the Maxwellian case. Specifically, the integrand can be expressed as its integral and residue portions

$$W_c^J(Z, \mathbf{p}_\perp) = (W_c^J)_I(Z, \mathbf{p}_\perp) + 2\pi i (W_c^J)_R(Z, \mathbf{p}_\perp) \quad (29a)$$

$$(W_c^J)_I(Z, \mathbf{p}_\perp) = \int_{-\infty}^{\infty} g_c^J(\xi_x; Z, \mathbf{p}_\perp) d\xi_x, \quad (29b)$$

$$(W_c^J)_R(Z, \mathbf{p}_\perp) = \begin{cases} A_J \frac{\bar{\xi}_x e^{c^2(1-\tilde{\gamma})}}{\tilde{\gamma} Q'(\bar{\xi}_x; \mathbf{p}_\perp)} & \Im(\bar{\xi}_x) < 0 \\ \frac{A_J}{2} \frac{\bar{\xi}_x e^{c^2(1-\tilde{\gamma})}}{\tilde{\gamma} Q'(\bar{\xi}_x; \mathbf{p}_\perp)} & \Im(\bar{\xi}_x) = 0 \\ 0 & \text{else} \end{cases} \quad (29c)$$

where $\bar{\xi}_x$ and Q' are as before. For the integral portion, the contour is again offset, and quadrature applied to obtain

$$W_c^J(Z, \mathbf{p}_\perp) \approx \begin{cases} \xi_{x+} T_{N_x}(-\tilde{g}_c^J(\xi_x; Z, \mathbf{p}_\perp, \eta_+)) + 2\pi i (W_c^J)_R(Z, \mathbf{p}_\perp) & \Im(z) \leq 0 \\ \xi_{x+} T_{N_x}(-\tilde{g}_c^J(\xi_x; Z, \mathbf{p}_\perp, \eta_-)) & \text{else.} \end{cases} \quad (30)$$

Again, in this formulation there are not separate cases for $\Im(Z) < 0$ and $\Im(Z) = 0$ because the line of integration avoids poles. Finally, the full dispersion function is evaluated as

$$D_c^J(\omega, k) \approx k^2 - \xi_{z+} T_{N_z} \left[\xi_{y+} T_{N_y} \left(W_c^J \left(\frac{\omega}{k}, [\xi_y, \xi_z] \right) \right) \right]. \quad (31)$$

For double precision accuracy it is again sufficient to take $\xi_{x\pm} = \xi_{y\pm} = \xi_{z\pm} = \pm 10$, and $N_x = N_y = N_z = 200$.

5.2.2. Sample Results for Maxwell-Jüttner Equilibrium

Similar to previous, application of the the formulation in (31) is used to evaluate the dispersion function with varying degrees of relativistic effects. Figure 8 presents the zero contours of the real and imaginary parts for $k = 1/3$ with $c = 8$ (strongly relativistic) and $c = 20$ (weakly relativistic) and should be compared against the Maxwellian equilibrium results in Figure 7. The spectrum of roots is again seen to form a hook terminating on the real axis at $\omega = ck$, but interestingly here there are apparently roots with $\Re(\omega) > ck$. This is a tantalizing observation is investigated in more depth in Section 7. Also as before, Newton's method is employed to compute the Landau roots, in the 3P case presented in Figure 8, as well as the 1P and 2P cases, with results presented in Table 2. Here the formulation of the reduced dimensionality Jüttner, and in particular its normalization, is slightly more involved than in the case of the Maxwellian, and the details are discussed in Appendix B. An interesting observation with respect to the results in Table 2 is that, unlike the case of a Maxwellian equilibrium, the dimensionality apparently effects primarily the frequency of the Landau root, with the effect on the damping rate rather minimal with no change in the first 5 significant figures.

6. Verification of Landau roots using kinetic simulation

The proposed methodology for evaluating the dispersion relation, and ultimately solving for the Landau roots, can be checked with respect to observed damping rates from kinetic simulation of the Vlasov-Poisson system. Similar checks have been used previously for code verification of kinetic simulation tools, e.g. [57, 62], a process which is essentially flipped here. Here, kinetic

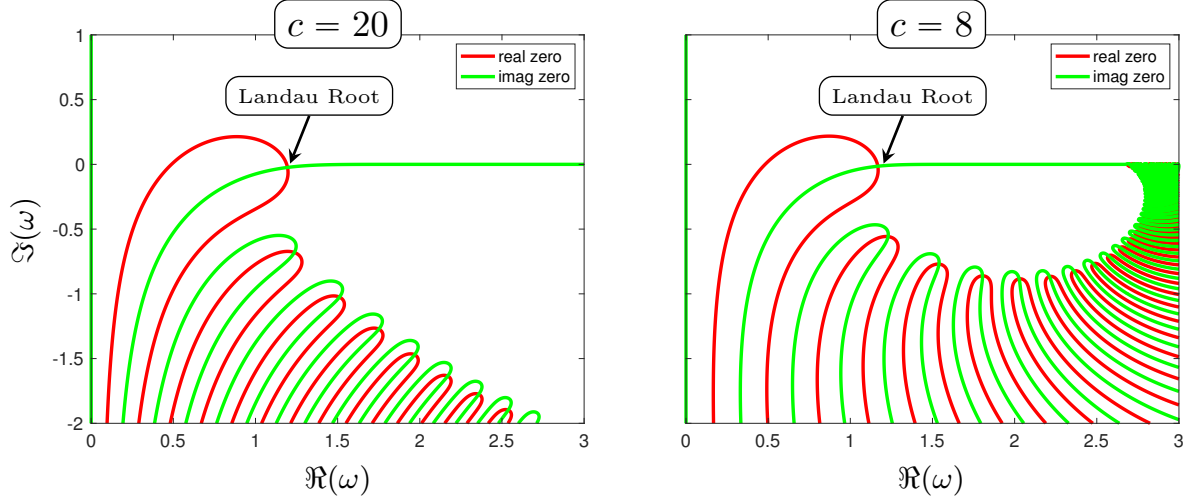


Figure 8: Zero contours of the real and imaginary parts of the relativistic dispersion relation with Maxwell-Jüttner equilibrium for $c = 20$ (left) and $c = 8$ (right). The spectrum of roots is again seen to form a hook which terminates on the real axis at $\omega = ck$. However, unlike the cases presented in Figure 7, the spectrum of roots is here seen to have elements with $\Re(\omega) > ck$. The location of the Landau root is also indicated, with the exact values listed in Table 2.

Jüttner		
	$c = 20$	$c = 8$
$d = 1$	$1.1962903 - i0.02381513$	$1.1760563 - i0.01443987$
$d = 2$	$1.1955483 - i0.02380358$	$1.1716859 - i0.01448172$
$d = 3$	$1.1948068 - i0.02379203$	$1.1673307 - i0.01452247$

Table 2: Table of Landau roots for Jüttner equilibrium in various momentum-space dimensions given by d with $c = 20$ (weakly relativistic) and $c = 8$ (strongly relativistic).

$c = 20$		
	Maxwellian	Jüttner
$d = 1$	1.195507 2723 $- i0.0230795$ 9656	1.196290 2892 $- i0.0238151$ 5141
$d = 2$	1.194520 5692 $- i0.0229827$ 4026	1.195548 2825 $- i0.0238035$ 9924
$d = 3$	1.193537 2407 $- i0.022886$ 40317	1.1948067 328 $- i0.0237920$ 4774

$c = 8$		
	Maxwellian	Jüttner
$d = 1$	1.17124 10154 $- i0.011332$ 34640	1.1760563 485 $- i0.0144$ 4002108
$d = 2$	1.165776 9434 $- i0.0111397$ 1856	1.1716859 793 $- i0.014481$ 86854
$d = 3$	1.16041 40933 $- i0.010948$ 86050	1.167330 6995 $- i0.014522$ 60369

Table 3: Tables extracted roots from kinetic simulation.

simulation results for Landau damping are obtained using a dimensionally generalized version of the LOKI code [62] which uses 6th-order accurate conservative finite differences with 6th-order accurate Runge-Kutta time stepping. These results are processed to extract both a frequency and damping rate, which are then compared to the theoretical results in Tables 1 and 2.

The computational setup, adapted from [62], uses an initial value problem in a single space dimension $x \in [-\frac{\pi}{k}, \frac{\pi}{k}]$, and d momentum dimensions $\mathbf{p} \in [-10, 10]^d$, with initial conditions

$$f(x, \mathbf{p}, t = 0) = f_E(\mathbf{p})(1 + \alpha \cos(kx)), \quad (32)$$

and $N_x = N_p = 80$ being the number of grid points in all dimensions. The wave number is taken to be $k = \frac{1}{3}$, and the magnitude of the initial perturbation is taken as $\alpha = 10^{-6}$ so that the dynamics are essentially linear. The simulation results are diagnosed in the traditional way by extracting a time trace of the standing wave electric field at a point. Due to linearity, the location of the extraction is immaterial (provided the location is not a zero of the standing wave). The damping rate is extracted by identifying local maxima of the time trace and then using a least squares fit in the log space to estimate the decay rate. The oscillation frequency is similarly determined, using the maxima of the time trace to obtain the oscillation frequency. For more details of the specifics of the data extraction used here see [62]. One challenge in this approach is isolating the behavior of the Landau root from other modes in the spectrum. As is typical, the approach used here simply waits sufficiently long so that the simulation contains essentially just the mode corresponding to the Landau root before beginning the data analysis. This is done by ignoring some of the first peaks in the data processing. However, one cannot wait arbitrarily long since the kinetic simulation will suffer from recurrence. Therefore, as discussed in [62], the precise selection of which peaks to consider is potentially delicate. In this work we choose to consider the 6th through 16th peaks, which appears to be sufficient for the present purposes. Results for this process applied to $c = 20$ and $c = 8$ for the Maxwellian and Jüttner in $d = 1, 2, 3$ appear in Table 3. Where these values differ from the corresponding theoretical values in Tables 1 and 2, the digits are colored red. The results indicate excellent agreement with roughly 5–8 digits of accuracy across all cases, which is in agreement with the limits of simulation diagnostics as discussed in [62]. Furthermore, the individual components of damping rate and frequency are independently in excellent agreement with their corresponding theoretical value.

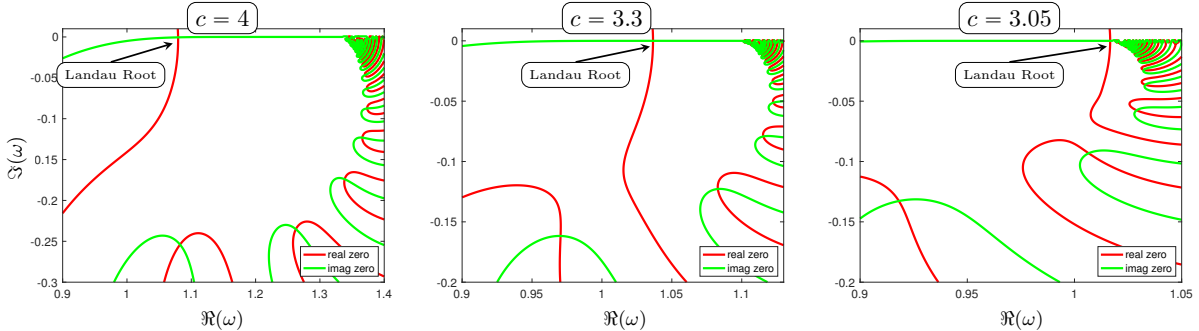


Figure 9: Zeros of the relativistic dispersion relation for the Jüttner equilibria with $c = 4$ (left), $c = 3.3$ (center), and $c = 3.05$ (right). Note that the plot limits change from left to right in an effort to keep the spectrum of roots within the field of view. From left to right one can observe the topology of the zero contours changing, specifically the zero real contour associated with the Landau root. Furthermore, moving from left to right the Landau root is approaching the terminus of the spectrum of roots at $\omega = ck$, and upon passing through it the Landau roots ceases to exist.

7. Landau damping in highly relativistic plasmas

The results in Sections 5.1.2 and 5.2.2 shows the dispersion relation contains roots that form a familiar “hook” terminating on the real axis at $\omega = ck$. However, the root identified as the Landau root does not appear to have a frequency that is overly sensitive to changing c (see Tables 1 and 2). These two observations naturally lead to the question of what happens as $c \rightarrow 1$, e.g. as the thermal velocity of a plasma approaches the speed of light. At the same time, Section 5.2.2 showed the existence of roots with $\Re(\omega) > ck$ for the case of the Jüttner equilibrium, adding additional intrigue to the question of what happens as $c \rightarrow 1$. As an illustration of the utility of the newly developed relativistic dispersion evaluator, this limit is now briefly investigated.

To begin addressing these questions, Figure 9 shows the zero contours of the real and imaginary parts of the dispersion relation with Jüttner equilibrium in the full 3-dimensional momentum space ($d = 3$) for $c = 4$, $c = 3.3$, and $c = 3.05$. Note that the qualitative picture is similar for reduced dimensionality, and even for Maxwellian equilibrium, although there are of course quantitative differences. The specific values for c are selected to highlight the changes in the spectrum of roots as c decreases and relativistic effects increase. Specifically, from $c = 4$ to $c = 3.3$, one can see that the root identified as the Landau root transitions from being the most slowly oscillating root, to the second-most slowly oscillating root. Furthermore, the topology of the real zero contour with respect to other contours changes as it moves left-to-right with increasingly strong relativistic effects. Subsequently in moving from $c = 3.3$ to $c = 3.05$, the the Landau root is effectively coincident with the terminus of the spectrum of roots at $\omega = ck$, and further increase in relativistic effects will result in the disappearance of the Landau root altogether. This last phenomenon will be investigated in more depth next.

To delve further into the behavior of the roots as relativistic effects become increasingly important, a simple continuation approach is used to trace various roots as functions of c . The continuation starts from $c = 20$ and the first 5 roots in the spectrum with respect to $|\omega|$ are tracked through to $c = 1.5$. This process is illustrated in the left panel of Figure 10 where the trajectories of the first 5 roots are shown on top of a dimmed version of the real and imaginary contours of the dispersion function for $c = 20$ (indicating the start of the continuation). The right two panels then show the real and imaginary parts of the traced roots as functions of c . The plot of the real part versus c also includes the reference line ck , indicating waves with a phase velocity equalling

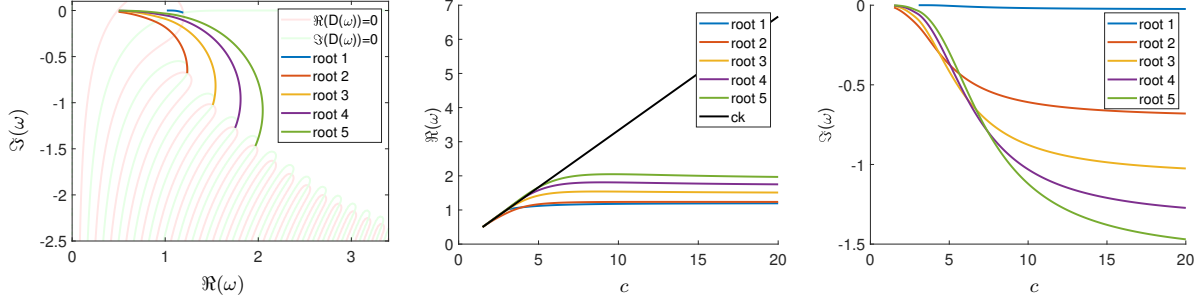


Figure 10: At right are trajectories of the first 5 roots starting at $c = 20$ and ending at $c = 1.5$. The real and imaginary zero contours of the dispersion function for $c = 20$ are shown dimly behind. At center is the real part of the first 5 roots as functions of c , and at right are the imaginary parts as functions of c .

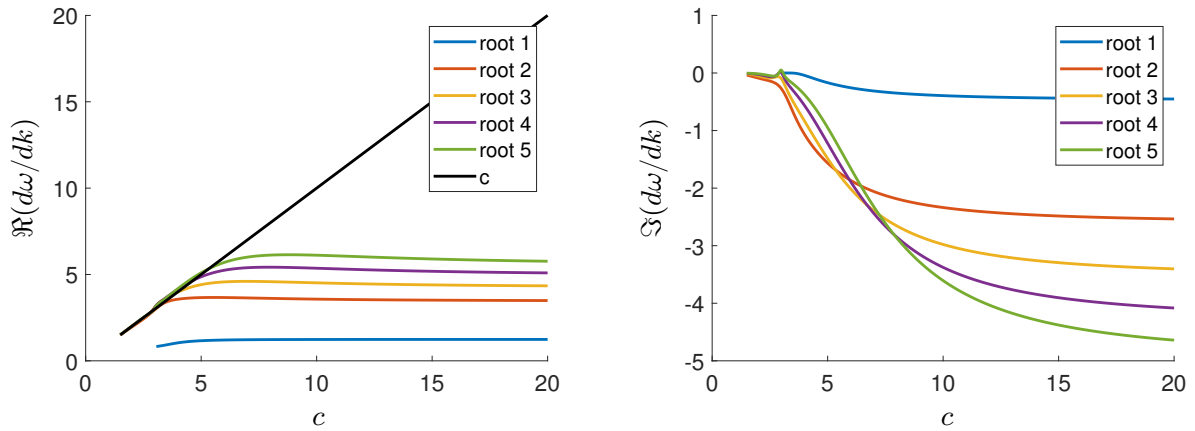


Figure 11: Real and imaginary parts of the phase velocity of the first 5 roots of the relativistic dispersion relation.

the speed of light. A keen observer may see that some of the roots exceed this phase velocity for $c \lesssim 4$ (see Figure 12 for more detail). Furthermore, the track of the imaginary roots vs c reveals that the Landau root (in blue) disappears for $c \approx 3.1$. This has significant practical implications since the remaining roots would then be significantly more strongly damped (albeit in an absolute sense the damping has already become quite small).

Continuing the investigation one step further, the phase velocity of the roots $d\omega/dk$ is computed along the trajectory from $c = 20$ to $c = 1.5$ using finite differences. Figure 11 shows both the real and imaginary parts of these computed phase velocities, with a phase speed equalling the speed of light also indicated in the plot of the real part. In agreement with [40], one can observe that there appear to be modes whose group velocity exceeds the speed of light. To be clear of this observation, Figure 12 shows the real parts of both $\omega - ck$ and $d\omega/dk - c$ so that positive numbers would indicate phase or group velocities exceeding the speed of light. Clearly both phase and group velocities do in fact exceed the speed of light. One interesting note is that for the Maxwellian equilibrium this observation is not true and neither the phase or group velocities exceed the speed of light.

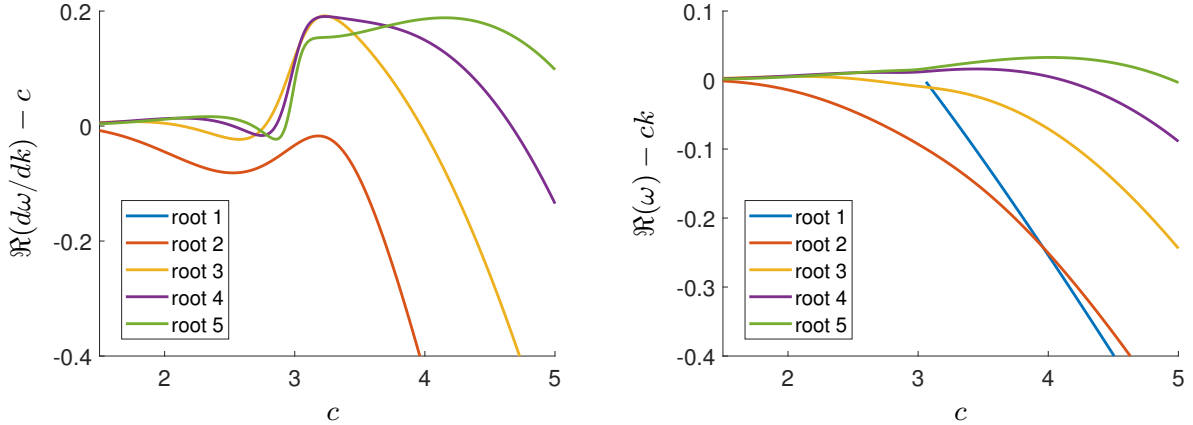


Figure 12: Real parts of $d\omega/dk - c$ and $\omega - ck$ for the first 5 roots of the relativistic dispersion relation.

8. Conclusions

In this manuscript we have developed a new approach to the evaluation of the relativistic dispersion relation for Langmuir waves. The basic idea is based on direct evaluation of the line integral after displacement in the complex plane so that numerical quadrature is more efficient. Simultaneously, the contribution from the pole associated with the deviation in the Landau contour is added analytically. The resulting method is shown to be accurate to machine precision for the non-relativistic case. Moving to the case of relativity, the computed roots of the dispersion relation are shown to be in excellent agreement with roots extracted from direct kinetic simulation. Finally, a showcase of the capability is provided by investigating the nature of the roots to the relativistic kinetic dispersion relation in the highly relativistic limit, and somewhat surprisingly there are apparently modes whose phase and group velocities exceed the speed of light.

Moving forward there are many interesting directions for follow on research. From the perspective of the physics, probing the existence of superluminal and/or undamped modes for the Vlasov-Poisson system is clearly very interesting. However, such investigation may be somewhat delicate since those modes with fastest group velocity are also the most highly damped. It may be possible to use external sources produced, for example, with beat waves to drive such waves. Further exploration of connections to solutions of the Lorentz invariant Vlasov-Maxwell system, as well as analysis of the Vlasov-Maxwell dispersion relation are also very promising routes that will be pursued in follow on work. From a computational perspective there are clear extensions to the capability, such as the use of other equilibrium distributions, e.g. those from experimental observation, or possessing flattened trapped particle regions. For example the distributions observed in experiments may appear Maxwell-Boltzmann at low velocity and power law or exponential at a higher temperature, or perhaps even double humped. Investigating such distributions may yield insights about the effects of damping in real-world experiments. To move to more exotic distributions, e.g. those with Heaviside step functions such as the incomplete Maxwellian, it may be fruitful to combine ideas presented in the present work with those of e.g. [42, 43, 81].

References

- [1] J. E. Ralph, A. Kemp, N. B. Meezan, R. L. Berger, D. Strozzi, B. J. MacGowan, O. Landen, N. Lemos, M. Belyaev, M. Biener, D. A. Callahan, T. Chapman, L. Divol, D. E. Hinkel,

- J. Moody, A. Nikroo, O. Jones, S. Schiaffino, M. Stadermann, P. Michel, "the effects of multi-species hohlraum walls on stimulated brillouin scattering, and hohlraum dynamics and beam propagation", *Phys. Plasmas* 28 (2021) 072704.
- [2] R. L. Berger, W. Arrighi, T. Chapman, A. Dimits, J. W. Banks, S. Brunner, The competing effects of wave amplitude and collisions on multi-ion species suppression of stimulated Brillouin scattering in inertial confinement fusion Hohlraums, *Physics of Plasmas* 30 (4) (2023) 042715.
- [3] E. Gibney, Nuclear-fusion reactor smashes energy record, *Nature* 602 (2022) 7897.
- [4] F. Eriksson, E. Fransson, M. Oberparleiter, H. Nordman, P. Strand, A. Salmi, T. Tala, J. Contributors, Interpretative and predictive modelling of joint european torus collisionality scans, *Plasma Physics and Controlled Fusion* 61 (11) (2019) 115004.
- [5] X. Xu, Y. Wang, F. Wei, X. Feng, X. Deng, Y. Ma, M. Zhou, Y. Pang, H.-C. Wong, Direct evidence for kinetic effects associated with solar wind reconnection, *Scientific Reports* 5 (2015) 8080.
- [6] S. Raptis, T. Karlsson, A. Vaivads, M. Lindberg, A. Johlander, H. Trollvik, On magnetosheath jet kinetic structure and plasma properties, *Geophysical Research Letters* 49 (21) (2022) e2022GL100678.
- [7] J. Luo, M. Chen, W. Y. Wu, S. M. Weng, Z. M. Sheng, C. B. Schroeder, D. A. Jaroszynski, E. Esarey, W. P. Leemans, W. B. Mori, J. Zhang, Multistage coupling of laser-wakefield accelerators with curved plasma channels, *Phys. Rev. Lett.* 120 (2018) 154801.
- [8] E. Esarey, C. B. Schroeder, W. P. Leemans, Physics of laser-driven plasma-based electron accelerators, *Rev. Mod. Phys.* 81 (2009) 1229–1285.
- [9] D. Lynden-Bell, The Stability and Vibrations of a Gas of Stars, *Monthly Notices of the Royal Astronomical Society* 124 (4) (1962) 279–296.
- [10] C. K. Birdsall, A. B. Langdon, *Plasma Physics via Computer Simulation*, Taylor and Francis, Boca Raton, 1991.
- [11] L. D. Landau, On the vibration of the electronic plasma, *J. Phys. (USSR)* 10 (1946) 25–34.
- [12] N. Van Kampen, On the theory of stationary waves in plasmas, *Physica* 21 (6) (1955) 949–963.
- [13] C. Mouhot, C. Villani, On Landau damping, *Acta Mathematica* 207 (2011) 29–201.
- [14] J. H. Malmberg, C. B. Wharton, Collisionless damping of electrostatic plasma waves, *Phys. Rev. Lett.* 13 (1964) 184–186.
- [15] T. M. O’Neil, Collisionless damping of nonlinear plasma oscillations, *Phys. Fluids* 8 (12) (1965) 2255–2262.
- [16] R. W. Gould, T. M. O’Neil, J. H. Malmberg, Plasma wave echo, *Phys. Rev. Lett.* 19 (1967) 219.
- [17] J. H. Malmberg, C. B. Wharton, R. W. Gould, T. M. O’Neil, Observation of plasma wave echoes, *Phys. Fluids*. 11 (1968) 1147.

- [18] P. T. Bonoli, Review of recent experimental and modeling progress in the lower hybrid range of frequencies at ITER relevant parameters, *Physics of Plasmas* 21 (6) (2014) 061508.
- [19] R. L. Berger, F. W. Perkins, Thresholds of parametric instabilities near the lower-hybrid frequency, *The Physics of Fluids* 19 (3) (1976) 406–411.
- [20] M. Porkolab, Parametric instabilities due to lower-hybrid radio frequency heating of tokamak plasmas, *The Physics of Fluids* 20 (12) (1977) 2058–2075.
- [21] N. J. Fisch, Confining a tokamak plasma with rf-driven currents, *Phys. Rev. Lett.* 41 (1978) 873–876.
- [22] F. Perkins, Heating tokamaks via the ion-cyclotron and ion-ion hybrid resonances, *Nuclear Fusion* 17 (6) (1977) 1197.
- [23] J. Hosea, S. Bernabei, P. Colestock, S. L. Davis, P. Efthimion, R. J. Goldston, D. Hwang, S. S. Medley, D. Mueller, J. Strachan, H. Thompson, Fast-wave heating of two-ion plasmas in the princeton large torus through minority-cyclotron-resonance damping, *Phys. Rev. Lett.* 43 (1979) 1802–1806.
- [24] M. N. Rosenbluth, Parametric instabilities in inhomogeneous media, *Phys. Rev. Lett.* 29 (1972) 565–567.
- [25] M. N. Rosenbluth, R. B. White, C. S. Liu, Temporal evolution of a three-wave parametric instability, *Phys. Rev. Lett.* 31 (1973) 1190–1193.
- [26] R. B. White, C. S. Liu, M. N. Rosenbluth, Parametric decay of obliquely incident radiation, *Phys. Rev. Lett.* 31 (1973) 520–523.
- [27] C. S. Liu, M. N. Rosenbluth, R. B. White, Parametric scattering instabilities in inhomogeneous plasmas, *Phys. Rev. Lett.* 31 (1973) 697–700.
- [28] N. Bertelli, O. Maj, E. Poli, R. Harvey, J. C. Wright, P. T. Bonoli, C. K. Phillips, A. P. Smirnov, E. Valeo, J. R. Wilson, Paraxial WentzelKramersBrillouin method applied to the lower hybrid wave propagation), *Physics of Plasmas* 19 (8) (2012) 082510.
- [29] J. D. Lindl, P. Amendt, R. L. Berger, S. G. Glendinning, S. H. Glenzer, S. W. Haan, R. L. Kauffman, O. L. Landen, L. J. Suter, The physics basis for ignition using indirect-drive targets on the National Ignition Facility, *Phys. Plasmas* 11 (2004) 339–491.
- [30] D. E. Hinkel, L. F. Berzak Hopkins, T. Ma, J. E. Ralph, F. Albert, L. R. Benedetti, P. M. Celliers, T. Döppner, C. S. Goyon, N. Izumi, L. C. Jarrott, S. F. Khan, J. L. Kline, A. L. Kritcher, G. A. Kyrala, S. R. Nagel, A. E. Pak, P. Patel, M. D. Rosen, J. R. Rygg, M. B. Schneider, D. P. Turnbull, C. B. Yeamans, D. A. Callahan, O. A. Hurricane, Development of improved radiation drive environment for high foot implosions at the national ignition facility, *Phys. Rev. Lett.* 117 (2016) 225002.
- [31] D. E. Hinkel, M. D. Rosen, E. A. Williams, A. B. Langdon, C. H. Still, D. A. Callahan, J. D. Moody, P. A. Michel, R. P. J. Town, R. A. London, S. H. Langer, Stimulated Raman scatter analyses of experiments conducted at the national ignition facility, *Phys. Plasmas* 18 (2011) 056312.

- [32] J. F. Myatt, J. Zhang, J. A. Delettrez, R. W. Short, W. Seka, D. H. Edgell, D. F. DuBois, D. A. Russell, H. X. Vu, The dynamics of hot-electron heating in direct-drive-implosion experiments caused by two-plasmon-decay instability, *Phys. Plasmas* 19 (2012) 022707.
- [33] R. S. Craxton, K. S. Anderson, T. R. Boehly, V. N. Goncharov, D. R. Harding, J. P. Knauer, R. L. McCrory, P. W. McKenty, D. D. Meyerhofer, J. F. Myatt, A. J. Schmitt, J. D. Sethian, R. W. Short, Direct-drive inertial confinement fusion: A review, *Phys. Plasmas* 22 (2015) 110501.
- [34] R. K. Follett, J. A. Delettrez, D. H. Edgell, V. N. Goncharov, R. J. Henchen, J. Katz, D. T. Michel, J. F. Myatt, J. Shaw, A. A. Solodov, C. Stoeckl, B. Yaakobi, , D. H. Froula, Two-plasmon decay mitigation in direct-drive inertial-confinement-fusion experiments using multi-layer targets, *Phys. Rev. Lett.* 116 (2016) 155002.
- [35] D. E. Hinkel, M. B. Schneider, B. K. Young, A. B. Langdon, E. A. Williams, M. D. Rosen, L. J. Suter, Creation of hot radiation environments in laser-driven targets, *Phys. Rev. Lett.* 96 (2006) 195001.
URL <https://link.aps.org/doi/10.1103/PhysRevLett.96.195001>
- [36] M. Schneider, D. Hinkel, S. Moon, S. Hansen, H. Baldis, C. Austrheim-Smith, G. Brown, K. Campbell, H.-K. Chung, K. Cone, C. Constantin, V. Glebov, J. Holder, G. Holland, D. James, A. Langdon, R. Lee, M. May, S. Roberts, B. Young, Development of a thermal x-radiation source using hot hohlraums, *High Energy Density Physics* 3 (2007) 256–262.
- [37] M. J. May, W. Farmer, N. Kostinsk, G. Kemp, P. Poole, P. Amendt, S. Brandon, M. Schneider, S. Prisbrey, B. Blue, Small scale hohlraums utility as a high fluence x-ray source, *Bull. Am. Phys. Soc.* (2006) TO08.00009.
- [38] A. Bers, I. P. Shkarofsky, M. Shoucri, Relativistic Landau damping of electron plasma waves in stimulated Raman scattering, *Physics of Plasmas* 16 (2) (2009) 022104.
- [39] B. Young, Landau damping in relativistic plasmas, *Journal of Mathematical Physics* 57 (2) (2016) 021502.
- [40] E. W. Laing, D. A. Diver, Relativistic Landau damping of longitudinal waves in isotropic pair plasmas, *Physics of Plasmas* 13 (9) (2006) 092115.
- [41] J. Bergman, B. Eliasson, Linear wave dispersion laws in unmagnetized relativistic plasma: Analytical and numerical results, *Physics of Plasmas* 8 (5) (2001) 1482–1492.
- [42] H.-S. Xie, Generalized plasma dispersion function: One-solve-all treatment, visualizations, and application to Landau damping, *Physics of Plasmas* 20 (9) (2013) 092125.
- [43] Y. Matsuda, G. R. Smith, A microinstability code for a uniform magnetized plasma with an arbitrary distribution function, *Journal of Computational Physics* 100 (2) (1992) 229–235.
- [44] P. Astfalk, F. Jenko, Leopard: A grid-based dispersion relation solver for arbitrary gyrotropic distributions, *Journal of Geophysical Research: Space Physics* 122 (1) (2017) 89–101.
- [45] D. Verscharen, K. Klein, B. Chandran, M. Stevens, C. Salem, S. Bale, Alps: the arbitrary linear plasma solver, *Journal of Plasma Physics* 84 (2018) 905840403.

- [46] T. Nakamura, T. Yabe, Cubic interpolated propagation scheme for solving the hyper-dimensional Vlasov-Poisson equation in phase space, *Comput. Phys. Commun.* 120 (1999) 122–154.
- [47] T. Nakamura, R. Tanaka, T. Yabe, K. Takizawa, Exactly conservative semi-Lagrangian scheme for multi-dimensional hyperbolic equations with directional splitting technique, *J. Comput. Phys.* 174 (2001) 171–207.
- [48] F. Filbet, E. Sonnendrücker, P. Bertrand, Conservative numerical schemes for the Vlasov equation, *J. Comput. Phys.* 172 (2001) 166–187.
- [49] L. Einkemmer, A performance comparison of semi-lagrangian discontinuous galerkin and spline based Vlasov solvers in four dimensions, *Journal of Computational Physics* 376 (2019) 937–951.
- [50] M. Gutnic, M. Haefele, I. Paun, E. Sonnendrücker, Vlasov simulations on an adaptive phase space mesh, *Comput. Phys. Commun.* 164 (2004) 214–219.
- [51] D. A. Silantyev, P. M. Lushnikov, H. A. Rose, Langmuir wave filamentation in the kinetic regime. i. filamentation instability of Bernstein-Greene-Kruskal modes in multidimensional Vlasov simulations, *Phys. Plasmas* 24 (2017) 042104.
- [52] D. A. Silantyev, P. M. Lushnikov, H. A. Rose, Langmuir wave filamentation in the kinetic regime. ii. weak and strong pumping of nonlinear electron plasma waves as the route to filamentation, *Phys. Plasmas* 24 (2017) 042105.
- [53] N. Besse, E. Sonnendrücker, Semi-Lagrangian schemes for the Vlasov equation on an unstructured mesh of phase space, *J. Comput. Phys.* 191 (2003) 341–376.
- [54] Y. Cheng, A. J. Christlieb, X. Zhong, Energy-conserving discontinuous Galerkin methods for the Vlasov-Maxwell system, *J. Comput. Phys.* 279 (2014) 145 – 173.
- [55] T. D. Arber, R. G. L. Vann, A critical comparison of Eulerian-grid-based Vlasov solvers, *J. Comput. Phys.* 180 (2002) 339–357.
- [56] F. Filbet, E. Sonnendrücker, Comparison of Eulerian Vlasov solvers, *Comput. Phys. Commun.* 150 (2003) 247–266.
- [57] J. W. Banks, J. A. F. Hittinger, A new class of non-linear, finite-volume methods for Vlasov simulation, *IEEE T. Plasma. Sci.* 38 (9) (2010) 2198–2207.
- [58] G. V. Vogman, U. Shumlak, P. Colella, Conservative fourth-order finite-volume Vlasov-Poisson solver for axisymmetric plasmas in cylindrical (r,vr,vz) phase space coordinates, *J. Comput. Phys.* 373 (2018) 877 – 899.
- [59] M. Kotschenreuther, G. Rewoldt, W. M. Tang, Comparison of initial value and eigenvalue codes for kinetic toroidal plasma instabilities, *Comput. Phys. Commun.* 88 (1995) 128–149.
- [60] W. Dorland, F. Jenko, M. Kotschenreuther, B. N. Rogers, Electron temperature gradient turbulence, *Phys. Rev. Lett.* 85 (26) (2000) 5579–5582.
- [61] J. Candy, R. E. Waltz, An Eulerian gyrokinetic-Maxwell solver, *J. Comput. Phys.* 182 (2) (2003) 545–581.

- [62] J. W. Banks, A. G. Odu, R. L. Berger, T. Chapman, W. T. Arrighi, S. Brunner, High-order accurate conservative finite difference methods for Vlasov equations in 2d+2v, *SIAM J. Sci. Comput.* 41 (2019) B953–B982.
- [63] J. W. Banks, R. L. Berger, S. Brunner, B. I. Cohen, J. A. F. Hittinger, Two-dimensional Vlasov simulation of electron plasma wave trapping, wavefront bowing, self-focusing, and sideloss, *Phys. Plasmas* 18 (5) (2011) 052102.
- [64] R. L. Berger, S. Brunner, J. W. Banks, B. I. Cohen, B. J. Winjum, Multi-dimensional Vlasov simulations and modeling of trapped-electron-driven filamentation of electron plasma waves, *Phys. Plasmas* 22 (2015) 055703.
- [65] C. Heerlein, G. Zwicknagel, Nonlinear Landau damping in spherically symmetric Vlasov Poisson systems, *Journal of Computational Physics* 180 (2) (2002) 497–505.
- [66] J.-M. Qiu, A. Christlieb, A conservative high order semi-lagrangian WENO method for the Vlasov equation, *Journal of Computational Physics* 229 (4) (2010) 1130–1149.
- [67] A. F. Vinas, A. J. Klimas, Flux-balance Vlasov simulation with filamentation filtration, *Journal of Computational Physics* 375 (2018) 983–1004.
- [68] Y. Li, Y. He, Y. Sun, J. Niesen, H. Qin, J. Liu, Solving the Vlasov-Maxwell equations using Hamiltonian splitting, *Journal of Computational Physics* 396 (2019) 381–399.
- [69] T. Yin, X. Zhong, Y. Wang, Highly efficient energy-conserving moment method for the multi-dimensional Vlasov-Maxwell system, *Journal of Computational Physics* 475 (2023) 111863.
- [70] N. J. Sircombe, T. D. Arber, VALIS: A split-conservative scheme for the relativistic 2D Vlasov-Maxwell system, *J. Comput. Phys.* 228 (13) (2009) 4773–4788.
- [71] A. Suzuki, T. Shigeyama, A conservative scheme for the relativistic Vlasov-Maxwell system, *Journal of Computational Physics* 229 (5) (2010) 1643–1660.
- [72] Y. Li, Energy conserving particle-in-cell methods for relativistic Vlasov-Maxwell equations of laser-plasma interaction, *Journal of Computational Physics* 473 (2023) 111733.
- [73] G. Chen, L. Chacon, L. Yin, B. Albright, D. Stark, R. Bird, A semi-implicit, energy- and charge-conserving particle-in-cell algorithm for the relativistic Vlasov-Maxwell equations, *Journal of Computational Physics* 407 (2020) 109228.
- [74] H. sheng Xie, Pdrf: A general dispersion relation solver for magnetized multi-fluid plasma, *Computer Physics Communications* 185 (2) (2014) 670–675.
- [75] S. Ichimaru, *Basic Principles of Plasma Physics: A Statistical Approach*, W. A. Benjamin Inc., London, 1973.
- [76] W. Gautschi, Efficient computation of the complex error function, *SIAM J. Numer. Anal.* 7 (1970) 187–198.
- [77] G. P. M. Poppe, C. M. J. Wijers, More efficient computation of the complex error function, *ACM Trans. Math. Softw.* 16 (1) (1990) 38–46.
- [78] J. A. C. Weideman, Computation of the complex error function, *SIAM J. Numer. Anal.* 31 (1994) 1497–1518.

- [79] M. R. Zaghoul, A. N. Ali, Computing the faddeyeva and voigt functions, *ACM Trans. Math. Softw.* 38 (2) (2011) 1–22.
- [80] L. N. Trefethen, J. A. C. Weideman, The exponentially convergent trapezoidal rule, *SIAM Rev.* 56 (2014) 385–458.
- [81] S. D. Baalrud, The incomplete plasma dispersion function: Properties and application to waves in bounded plasmas, *Physics of Plasmas* 20 (1) (2013) 012118.
- [82] R. L. Berger, C. H. Still, E. A. Williams, A. B. Langdon, On the dominant and subdominant behavior of stimulated Raman and Brillouin scattering driven by nonuniform laser beams, *Physics of Plasmas* 5 (12) (1998) 4337–4356.
- [83] D. J. Strozzi, D. S. Bailey, P. Michel, L. Divol, S. M. Sepke, G. D. Kerbel, C. A. Thomas, J. E. Ralph, J. D. Moody, M. B. Schneider, Interplay of laser-plasma interactions and inertial fusion hydrodynamics, *Phys. Rev. Lett.* 118 (2017) 025002.
- [84] R. A. Treumann, W. Baumjohann, Anisotropic Jüttner (relativistic Boltzmann) distribution, *Ann. Geophys.* 34 (2016) 737–738.
- [85] G. Livadiotis, Modeling anisotropic Maxwell-Jüttner distributions: derivation and properties, *Ann. Geophys.* 34 (2016) 1145–1158.

Appendix A. Order of integration in the multi-dimensional dispersion function

When solving the integral in the relativistic dispersion relation for dimensions higher than one, it is important to note here that the appearance of the residue, e.g. in Equation (24), leading to the implementable explicit formulation, e.g. in Equation (21c) is only possible if one integrates over p_x first. If one instead integrates over other momenta dimensions first, the numerical quadrature leaves the form of the resulting residue unclear.

For example, supposing one wishes to integrate the function $g(x, y)$, which contains a singularity treated with the Landau contour in the x -dimension. Now assuming one chooses to integrate over y first, the integral would be $\int_{\Gamma} \int_{\xi_{y-}^{\xi_{y+}}} g(x, y) dy dx$. Using the trapezoidal approximation methods outlined in Equation (13b), the integrand would become $\int_{\Gamma} \left[\int_{\xi_{y-}^{\xi_{y+}}} T_{N_y}(g(x, y)) \right] dx$. Unfortunately now the integrand for the Landau contour is a discrete function sampled on a grid. As a result it is unclear how to identify the form of the pole and subsequently incorporate it into the formulation. On the contrary, if integrating over x first, the formulation becomes as discussed and incorporation of the effect of the pole is straight forward.

Appendix B. General form of the Jüttner normalization factor

A general form for the normalization of a Jüttner equilibrium function is outlined in detail in [41] and [84]. The general d -dimensional anisotropic Jüttner is expressed as

$$f_J^{(d)}(\mathbf{p}) = \left(\prod_{j=1}^d \alpha_j \right) A_J^{(d)} e^{c^2(1-\gamma_d)}, \quad (\text{B.1a})$$

with multidimensional, anisotropic Lorentz factor

$$\gamma_d = \sqrt{1 + \frac{\sum_{j=1}^d (p_j \alpha_j)^2}{c^2}}. \quad (\text{B.1b})$$

Recall that Section 5 discusses the appearance of the “extra” factor of e^{c^2} to avoid numerical overflow. The normalization factor must then be computed to ensure $\int_{-\infty}^{\infty} f_J^{(d)}(\mathbf{p}) d\mathbf{p} = 1$, which implies

$$A_J^{(d)} = (2\pi)^{\frac{1-d}{2}} \frac{1}{2ce^{c^2}} \frac{1}{K_{\frac{d+1}{2}}(c^2)}, \quad (\text{B.2})$$

where $K_\nu(\cdot)$ is the modified Bessel function of the second kind of order ν . To avoid numerical issues associated with evaluating e^{c^2} , care must be exercised when evaluating $A_J^{(d)}$ for large c . However, note that for even dimension the entirety of the expression B.2 simplifies drastically and the issue is avoided.

For completeness, for $d = 1$,

$$A_J^{(1)} = \begin{cases} \frac{1}{2ce^{c^2} K_1(c^2)} & \text{if } |c| < 10 \\ (2\pi)^{-\frac{1}{2}} E_1 & \text{else} \end{cases} \quad (\text{B.3})$$

where

$$E_1 = 1 - \frac{3}{8c^2} + \frac{33}{128c^4} - \frac{249}{1024c^6} + \frac{9963}{32768c^8} - \frac{131229}{262144c^{10}} + \frac{4471749}{4194304c^{12}} - \frac{95412897}{33554432c^{14}} + \frac{19670636403}{2147483648c^{16}} - \frac{593441620209}{17179869184c^{18}} + \mathcal{O}(c^{-20}). \quad (\text{B.4})$$

For $d = 2$, there is no need to perform an asymptotic expansion due to the nice representation of the half-integer Bessel functions and one obtains

$$A_J^{(2)} = \frac{c^2}{2\pi(1+c^2)}. \quad (\text{B.5})$$

The case of $d = 3$ is treated in the Section 5.2.